



PHOTOANODE OF DYE-SENSITIZED SOLAR CELLS BASED ON TITANIUM DIOXIDE WITH REDUCED GRAPHENE OXIDE

Leszek Adam Dobrzański¹, Marzena Prokopiuk vel Prokopowicz^{1,*}, Peter Palček², Aleksandra Drygała³, Krzysztof Lukaszewicz⁴, Mariusz Król

¹ Division of Materials Processing Technology, Management, and Computer Techniques in Materials Science, Institute of Engineering Materials and Biomaterials, Silesian University of Technology, 44-100 Gliwice, Konarskiego 18a St. Poland

² Department of Materials Engineering, Faculty of Mechanical Engineering, University of Žilina, Univerzitná 1, 010 16 Žilina, Slovak Republic

³ Division of Metal and Plastic Processing, Institute of Engineering Materials and Biomaterials, Silesian University of Technology, 44-100 Gliwice, Konarskiego 18a St. Poland

⁴ Division of Nanocrystalline and Functional Materials and Sustainable Proecological Technologies, Institute of Engineering Materials and Biomaterials, Silesian University of Technology, 44-100 Gliwice, Konarskiego 18a St. Poland

*corresponding author: e-mail: marzena.pvp@gmail.com

Resume

Dye-sensitized solar cells are one of the most promising new generation of photovoltaic cells due to their low cost, easy fabrication and high energy conversion. One of the key components of DSSC is photoanode that supports dye molecules and helps in the electron transfer. Titanium dioxide film used as a photoanode should have nanocrystalline structure, mesoporous nature and be semi-transparent. A thin semiconductor layer consist of nanocrystalline grains, therefore, DSSCs are also called nanocrystalline solar cells. Transparency is also an important issue of photovoltaic cells, especially when used in building integrated photovoltaics (BIPV) on glass and metal substrates. Moreover, the transparency allows their use in tandem cells.

The paper presents the results of the structure investigation, optical and electrical properties of a photoanode in dye-sensitized solar cells with reduced graphene oxide in the structure of photoanode. Photoanode with rGO achieve the conversion efficiency of 4.5 % while standard DSSC achieves 4.3 %. A dye-sensitized solar cells with reduced graphene oxide exhibit greater light-harvesting efficiency and absorbance in comparison to photoanode without reduced graphene oxide. Using a reduced graphene oxide in photoanode of dye-sensitized solar cell allows to produce two dimensional structures between nanoparticles of titanium dioxide, that increase rate of electron transport and reduce recombination in DSSCs.

Article info

Article history:

Received 30 June 2016

Accepted 02 January 2017

Online 27 February 2017

Keywords:

Dye-sensitized solar cells;
Photoanode;
Titanium dioxide;
Nanocrystalline films;
Transparency.

Available online: <http://fstroj.uniza.sk/journal-mi/PDF/2016/01-2017.pdf>

ISSN 1335-0803 (print version)

ISSN 1338-6174 (online version)

1. Introduction

The environmental issues such as ozone hole, acid rain, greenhouse effect, etc., affect every human, animal and nation on this planet and are a threat to both health and life. They result from, among other factors, mass burning of fossil fuels such as coal and oil. In the common perception fossil fuels will be replaced by cleaner and cheaper renewable

energy sources, the use of which is not associated with long-term deficits, because their supply is renewed in a short time. Humanity consumes enormous amounts of energy resources, and most of this energy come from fossil fuels (Fig. 1). The growing public awareness that oil reserves on Earth can be exhausted as early as in this century also drives the development of renewables [1, 2].

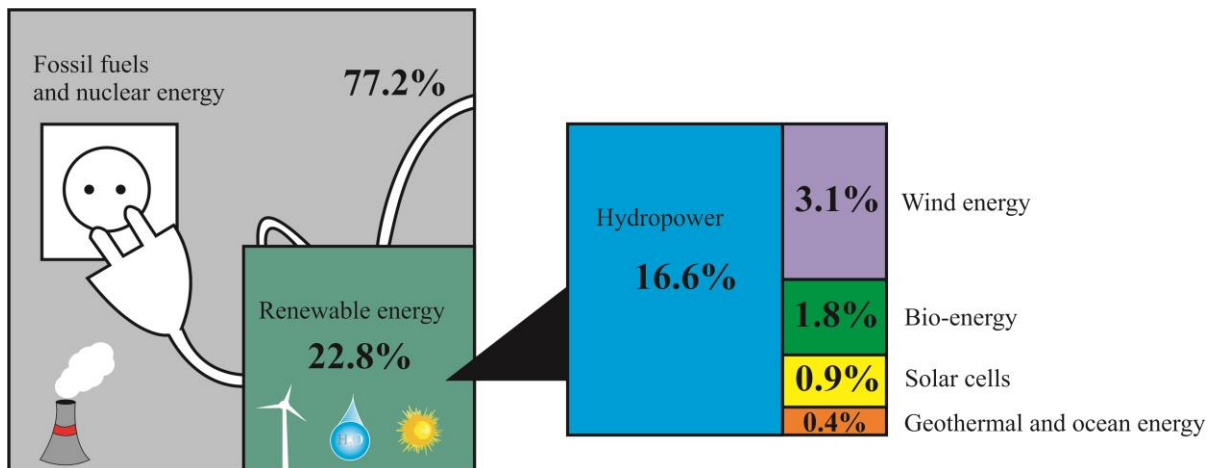


Fig. 1. World production of electricity in 2013 [1, 2].
(full colour version available online)

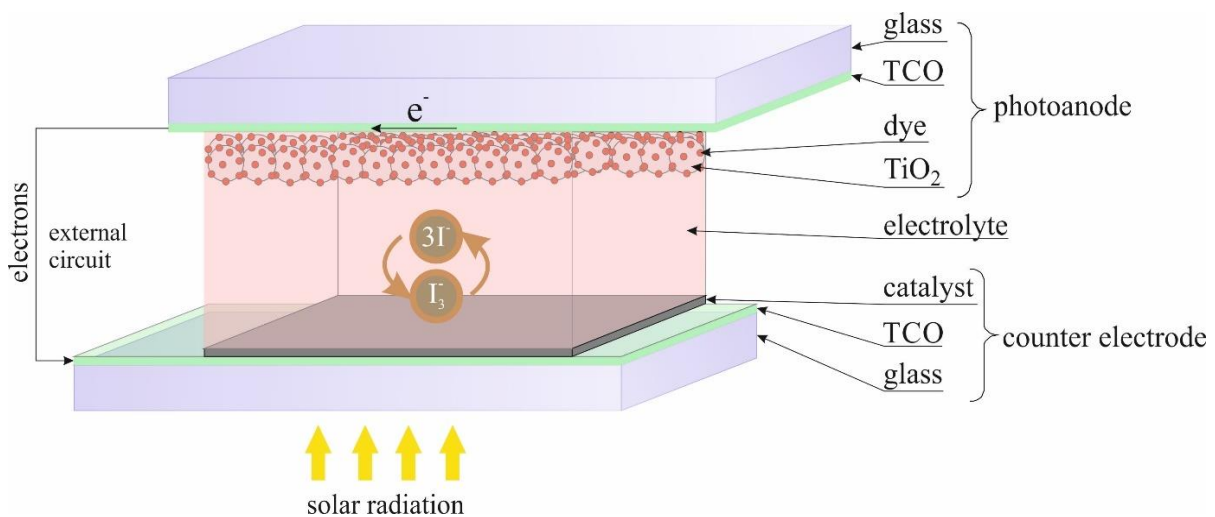


Fig. 2. Schematic of construction and operation principle of dye-sensitized solar cells.
(full colour version available online)

A lot of interest in renewable energy sources enjoys the solar energy. To convert sunlight into electrical power are used photovoltaic cells [3 - 5].

Today's photovoltaic market is dominated by photovoltaic solar cells with a p-n junction between solid state inorganic materials, usually from a crystalline or amorphous silicon, using the experience of very well-developed electronics industry. Silicon solar cells account for over 80 % of the photovoltaic industry [3 - 5]. In the recent years, this domination was disturbed by the emergence of photovoltaic cells based on nanocrystalline materials and conductive polymer films. This type of photovoltaic cells offers the prospect of low-cost production with a combination of various

attractive features like flexibility, transparency and lack of toxicity of mainly used materials [3, 6]. It is possible to complete separation of the semiconductor junction devices by replacing the contact phase of the semiconductor through the electrolyte, resulting in a photoelectrochemical cell. Contrary to expectations, the devices based on interpenetrating networks of mesoscopic semiconductor show a surprisingly high conversion efficiency (14 % in the laboratory) [7] so that they can compete with conventional solar cells. One example of this type of the solar cell is a dye-sensitized solar cell (DSSC) in which the optical absorption and charge separation process is achieved through the use of the dye as the material absorbing light from

a nanocrystalline semiconductor with a wide energy band gap [6 - 10]. Usually, a DSSC is composed of transparent conductive oxide (TCO) coated glass, a nanoporous titanium dioxide film with absorbed dye, a counter electrode and a liquid electrolyte containing iodide/triiodide redox couple. In Fig. 2 schematics of the construction and operation principle of DSSC is shown.

One of the key components of DSSC is a photoanode that supports dye molecules and helps in the electron transfer. The titanium dioxide film used as a photoanode should have a nanocrystalline structure, a mesoporous nature and be semi-transparent [10, 11]. A thin semiconductor layer contains nanocrystalline grains. Therefore, DSSCs are also called nanocrystalline solar cells. Compounds such as titanium dioxide, zinc oxide, tin oxide, niobium oxide, zirconium oxide can be used as semiconductors in a photoanode. The titanium dioxide is the most commonly used due to its excellent structural stability in solutions and during solar radiation, as well as light sensitivity and low price [11]; it is a widely available non-toxic material used in everyday products as toothpaste, sun-protection creams or paint. It comes in three natural forms: rutile, anatase and brookite. Dye-sensitized solar cells require the most active form of titanium dioxide – polymorphic anatase due to its relatively high energy band gap and high energy of conduction band edge. Anatase is an n-type semiconductor with energy band gap equal to 3.2 eV, which corresponds to the optical onset of approximately 390 nm to light absorption. Conventional crystalline silicon solar cells require silicon purity of 99.9999 % (less than 1 ppm total impurities). Requirements for anatase in the dye-sensitized cells are less stringent but nevertheless significant. The high-quality batch of titanium oxide as the one used in the commercial production of titanium dioxide paste has a phase purity of at least 99 %. Currently, the most popular paste of titanium dioxide available

on the market contains 80 % anatase and 20 % rutile [12, 13].

Because of the wide band gap (~ 3.2 eV), titanium dioxide only absorbs UV light, including a small fraction (~ 5 %) of the solar spectrum. The organic compounds which absorb visible radiation are used as dyes in the dye-sensitized solar cells due to their stability in the presence of light and have groups which allow the permanent bonding of the semiconductor surface. Natural dyes, such as chlorophyll, carotene and anthocyanins are widely available in plants, flowers and fruit. In the laboratory, dye-sensitized solar cells based on natural dyes reached an efficiency of 7.1 % [14]. Because of their high absorption of visible light, a long lifetime after excitation and the effectiveness of charge transfer metal - ligand most often used are ruthenium-based N3, N719 and Z-907 dyes [13 - 15].

Transparency is also an important issue of photovoltaic cells, especially when used in building integrated photovoltaics (BIPV) on glass and metal substrates. Moreover, the transparency allows their use in tandem cells [16].

One of the promising methods for increasing the collection efficiency of the charge in dye-sensitized solar cells is changing the morphology of the titanium dioxide by using a mixture of titanium dioxide with highly conductive carbon materials. Among various carbon materials, to enhance the electron transport and thereby increase the efficiency of the dye-sensitized solar cell, reduced graphene oxide have been used. Using a reduced graphene oxide rGO in photoanode of dye-sensitized solar cell allows to produce two dimensional structures between nanoparticles of titanium dioxide, that increase rate of electron transport and reduce recombination in DSSCs.

The primary objective of this work is to present the results of the structure investigation of a photoanode in dye-sensitized solar cells using the titanium dioxide with

reduced graphene oxide and N3 dye by using scanning electron microscope and X-ray diffraction. The effect of N3 dyes and titanium dioxide layers on absorbance, transmittance and light harvesting efficiency, was investigated. The electrical properties of dye-sensitized solar cells were measured.

2. Experimental

2.1 Materials

The FTO (fluorine-doped tin oxide) glass substrates ($10 \Omega \cdot \text{sq}^{-1}$, 3D Nano) were cut into pieces with a size of $2.5 \times 2.5 \text{ cm}^2$ and ultrasonically cleaned in distilled water, acetone and ethanol for 15 min, respectively.

Ruthenium dye N3 - Cis-diisothiocyanato-bis(2,2'-bipyridyl-4,4'-dicarboxylic acid) ruthenium(II), Iodolyte electrolyte and highly dispersed titania nanoparticle paste for the photoanode were purchased from Solaronix (Switzerland). The platinum paste was purchased from 3D Nano (Poland). The graphene oxide was obtained from CheapTubes. Reduced graphene oxide was prepared according to the procedure in previous work [18].

2.2 Photoanode preparations

The productions steps of photoanode preparations are shown in Fig. 3. In order to prepare photoanode with reduced graphene oxide to the titanium dioxide paste was added

5% wt. of reduced graphene. Three layers of titanium dioxide with or without reduced graphene oxide were screen printed on previously cleaned FTO glass or glass without FTO (Fig. 3a), and each one was dried at 105°C . Then the films were annealed in an air stream at 500°C for 30 min (Fig. 3b), cooled down to 80°C , and then placed in the anhydrous ethanol solution of 0.5 mM. N3 dye for 24 h and without access to light (Fig. 3c). Once removed, the electrode was washed with ethanol to remove excess dye and allowed to dry.

2.3 Dye-sensitized solar cells preparation

Dye-sensitized solar cells were made by combining the platinum counter electrode (screen printed on FTO glass and annealed in 500°C for 30 min) and the photoanode. The space between electrode was filled with high-performance electrolyte with high-concentration of triiodide (from Solaronix).

2.4 Measurements

Scanning Electron Microscopic (SEM) images were taken with a Zeiss Supra 35. The X-ray Diffraction (XRD) analysis was recorded on a Panalytical X'Pert Pro diffractometer using filtered radiation from the lamp with copper anode. X-ray phase analysis was performed in the Bragg-Brentano geometry by using X'celerator strip detector.

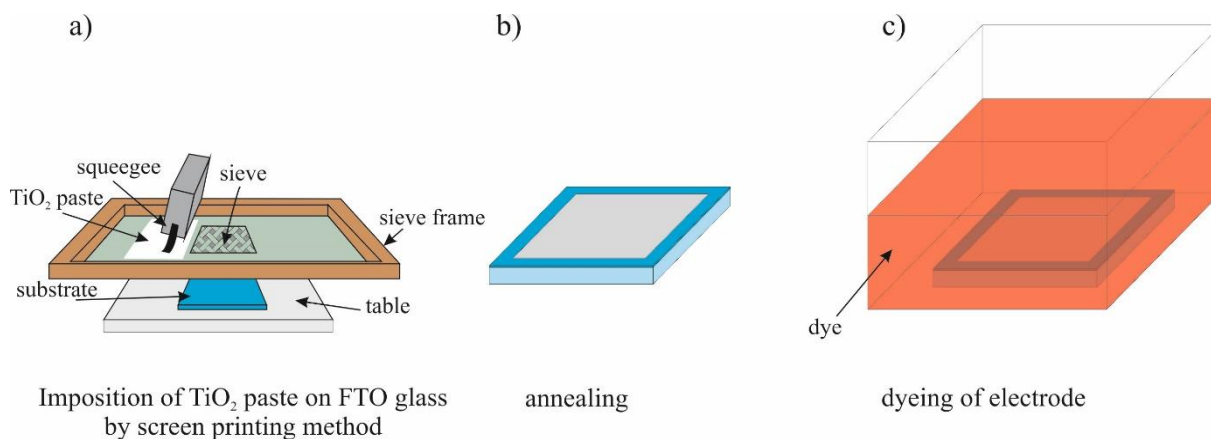


Fig. 3. Schematic of photoanode production steps in dye-sensitized solar cells. (full colour version available online)

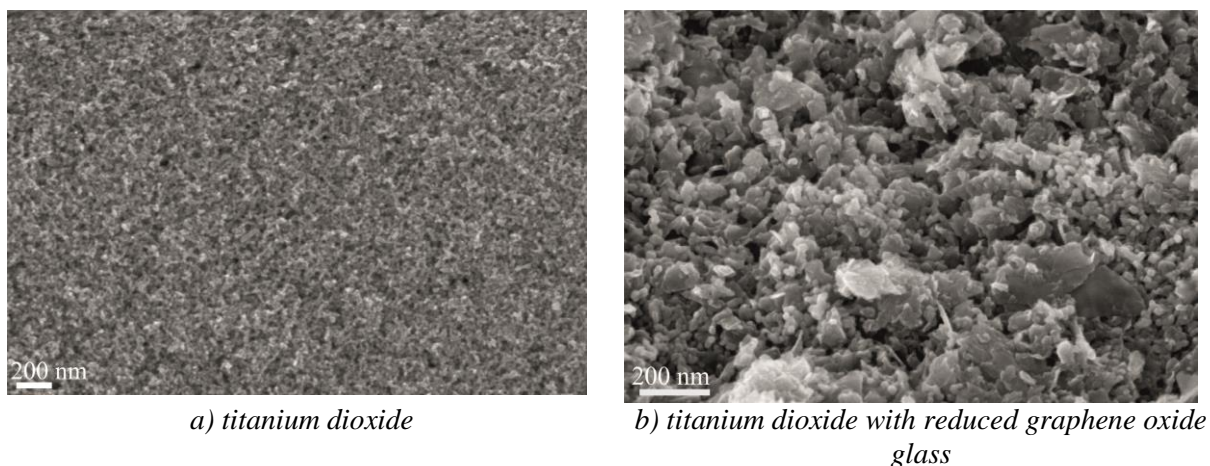


Fig. 4. The morphology of a) titanium dioxide b) titanium dioxide with reduced graphene oxide on glass after sintering, SEM.

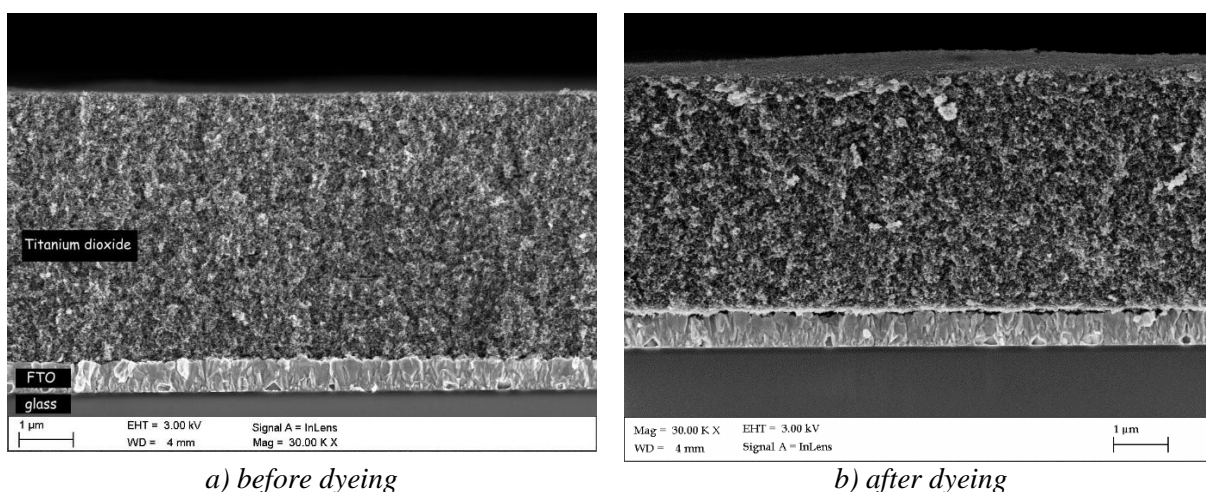


Fig. 5. Cross-section of FTO glass coated with titanium dioxide before a) and after b) dyeing, SEM.

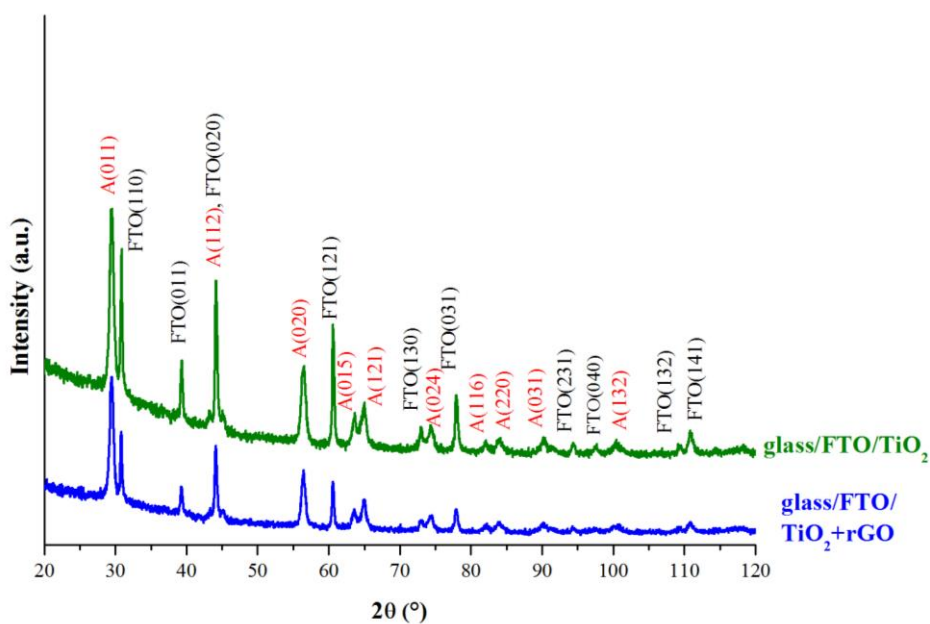


Fig. 6. X-ray diffraction pattern of titanium dioxide layer with and without reduced graphene oxide, where: A - nanocrystalline anatase, glass/FTO - glass substrate coated with FTO, rGO - reduced graphene oxide. (full colour version available online)

The transmittance and absorbance of titanium dioxide layers with and without dye and reduced graphene oxide were measured by Thermo Scientific Evolution 220 spectrophotometer equipped with a xenon lamp in the wavelength range from 190 nm to 1100 nm. Light harvesting efficiency *LHE* was calculated using the following formula [18]:

$$LHE(\lambda) = (1 - 10^{-A(\lambda)}) \cdot 100 \quad (1)$$

where $A(\lambda)$ is the absorbance at a specific wavelength.

The studies of electrical properties of experimentally prepared dye-sensitized solar cells containing in its photoanode reduced graphene oxide were performed on a computerized station SS IV CT-02 for measurement of current-voltage (IV) characteristics equipped with AAA sunlight simulator and with low current meter - Keithley 2401 for dye-sensitized photovoltaic cells measurement.

3. Description of achieved results

Fig. 4 shows the SEM images of FTO glass coated with titanium dioxide with and without reduced graphene oxide after sintering at 500°C. Fig. 5a and Fig. 5b show SEM images of cross section of FTO glass coated with titanium dioxide before and after dyeing. The thickness of titanium dioxide layer was measured by SEM to be ~14.92 μm. It can be seen that uniform structure of titanium dioxide film was obtained by screen printing method. Between the reduced graphene oxide and titanium oxide exists good contact. Moreover reduced graphene oxide is consistently distributed in the photoanode.

Fig. 6 shows the X-ray diffraction pattern of titanium dioxide on the FTO glass. The presence of only anatase form of titanium dioxide indicates a high quality of paste. Due to the transparency of titanium dioxide layer on X-ray diffraction pattern, some peaks from FTO can be seen. Reduced graphene oxide due

to its small share in photoanode does not change the phase composition of the material.

Fig. 7 shows the transmittance of particular layers of photoanode in dye-sensitized solar cells. The best transmittance has the pure glass covered with FTO. At a range of 300 – 400 nm within the ultraviolet region, the dye as well as the TiO₂ coated FTO glass exhibited a low value of transmittance but increased gradually through the visible region and obtained maximum values in the infrared region. It can be observed that the transmittance of all samples without reduced graphene oxide was over 70 % of the wavelength between 700 and 1000 nm. In the case of photoanode with reduced graphene oxide, the maximum transmittance was 60 % which indicates on increased absorption of solar radiation.

The absorbance of particular layers in photoanode is presented in Fig. 8. The best absorbance has titanium dioxide with reduced graphene oxide coated FTO glass with absorbed dye. It confirms the importance of dye in DSSC cells and its high absorption of visible light. Besides the optical absorbance and transmittance spectra, LHEs were also calculated for the 200 - 1100 nm wavelength. Fig. 9 shows a light harvesting efficiency of each layer in photoanode. The dye increases the light harvesting efficiency of the wavelength 400 - 600 nm. It can be seen that FTO also affects the light harvesting efficiency when moved towards the visible light. Furthermore, photoanode with a reduced graphene oxide is able to absorb more solar radiation than photoanode without reduced graphene oxide, increasing energy conversion efficiency of solar radiation into electrical energy. This is due to the fact that between the particles of titanium dioxide, by using of the reduced graphene oxide, two-dimensional structures are formed, which provide faster electrons transport to the FTO layer, and thereby they are reducing the degree of recombination of the excited electron with the triiodide anion from the electrolyte.

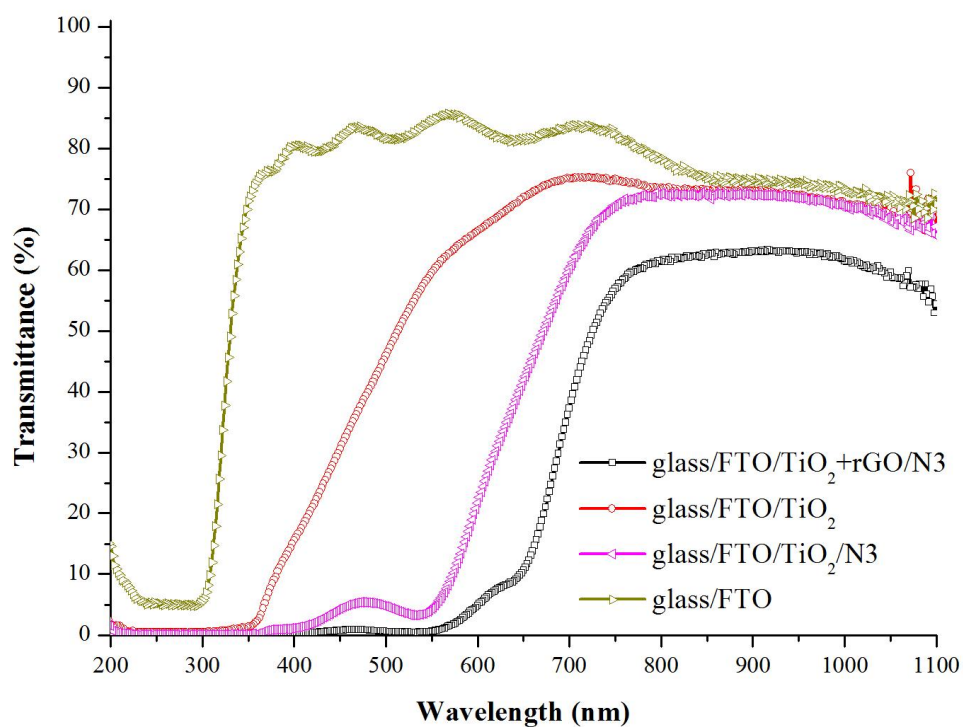


Fig. 7. Transmittance of particular layer of photoanode, where: glass/FTO - glass substrate coated with FTO, TiO₂+rGO - titanium dioxide with reduced graphene oxide, N3 - dye.
(full colour version available online)

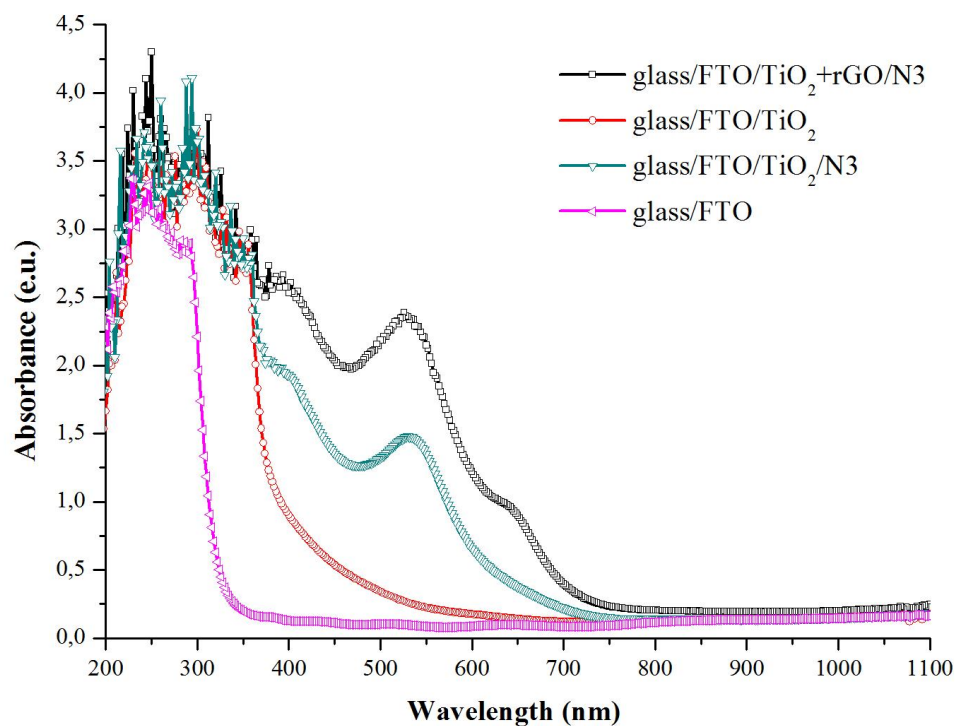


Fig. 8. Absorbance of each layer of photoanode, where: glass/FTO - glass substrate coated with FTO, TiO₂+rGO - titanium dioxide with reduced graphene oxide, N3 - dye.
(full colour version available online)

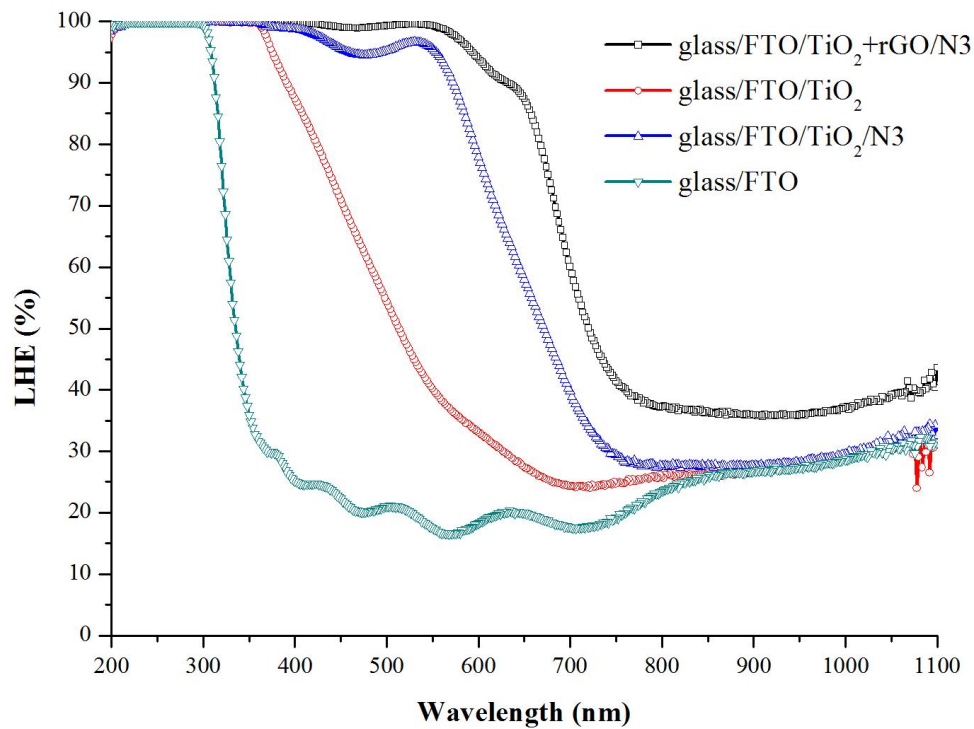


Fig. 9. Light harvesting efficiency LHE of particular layer of photoanode, where: glass/FTO - glass substrate coated with FTO, TiO₂+rGO - titanium dioxide with reduced graphene oxide, N3 - dye. (full colour version available online)

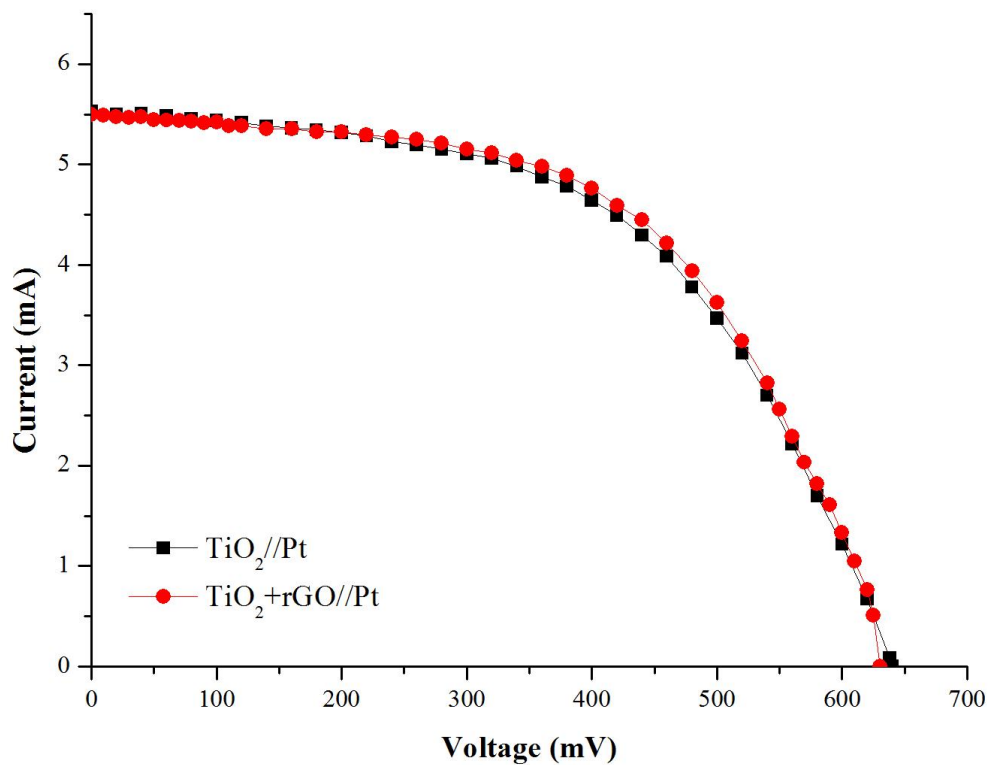


Fig. 10. Current-voltage characteristics of dye-sensitized solar cells. (full colour version available online)

The current-voltage characteristics of prepared dye-sensitized solar cells with and without reduced graphene oxide in photoanode are shown in Fig. 10. DSSC with standard photoanode shows an open circuit voltage (U_{oc}) of 0.64 V and the short circuit current (I_{sc}) of 5.4 mA with conversion efficiency (η) of 4.3 %. Upon loading the reduced graphene oxide to photoanode, DSSC yielded an I_{sc} of 5.5 mA, U_{oc} of 0.64V and η of 4.5 %. The achieved results can be compared to the data reported by Menghua Zhu in [18] where conversion efficiency of 4.28 % was achieved. Compared to that, the applied screen printing method in the production of photoanode shows simplicity and dye-sensitized solar cells with higher efficiency can be obtained.

4. Conclusions

In conclusion, we demonstrated the titanium dioxide with reduced graphene oxide layers preparing by screen printing method on FTO glass, followed by being sensitized in the N3 dye. It was shown that uniform structure of titanium dioxide photoanode was obtained. In the case of titanium dioxide with reduced graphene oxide it was shown that reduced graphene oxide is consistently distributed in the photoanode. Because of its high transmittance, it is possible to use dye-sensitized solar cells in building integrated photovoltaic. Absorbance, as well as light harvesting efficiency is higher for photoanode with reduced graphene oxide. It indicates stronger absorption in visible light for titanium dioxide with reduced graphene oxide coated FTO glass with dye. The higher conversion efficiency for DSSC with rGO indicates on the higher transfer of electrons between the titanium dioxide and FTO.

Acknowledgements

The project was partially funded by the National Science Centre by the contract No. DEC-2013/09/B/ST8/02943.

Marzena Prokopiuk vel Prokopowicz was a holder of the scholarship from the International Visegrad Fund.

References

- [1] H. Ellis: Characterization of dye-sensitized solar cells. Components for environmentally friendly photovoltaics, Uppsala University, Dissertation for the Licentiate of Philosophy in Physical Chemistry.
- [2] Renewables 2015 global status report. Technical report, REN21, 2015.
- [3] M. Grätzel: Nature 414 (2001) 338-344.
- [4] L.A. Dobrzański, A. Drygała: Journal of Achievements in Materials and Manufacturing Engineering 31(1) (2008) 77-82.
- [5] L.A. Dobrzański, A. Drygała, M. Prokopiuk vel Prokopowicz: Arch. Mater. Sci. Eng. 62(2) (2013) 53-59.
- [6] Y. Jiao, F. Zhang, S. Meng, L.A. Kosyachenko (Ed.): Dye Sensitized Solar Cells Principles and New Design, Solar Cells - Dye-Sensitized Devices, ISBN: 978-953-307-735-2, In Tech 09 (2011).
- [7] K. Kakiage, Y. Aoyama, T. Yano, K. Oya, J. Fujisawa, M. Hanaya: Chem. Commun. 51 (2015) 15894–15897.
- [8] J. Gong, J. Liang, K. Sumathy: Renew. Sust. Energ. Rev. 16 (2012) 5848-5860.
- [9] M. Grätzel: Review: Journal of Photochemistry and Photobiology C: Photochemistry Reviews 4 (2003) 145-153.
- [10] A. Ariyarat, K. Manabe, K. Fukada, K-H. Kyung, K. Fujimoto, S. Shiratori: Royal Society of Chemistry Advances 5 (2015) 52427-52435.
- [11] M. Sokolsky, J. Cirak: Acta Electrochnica et Informatica 10(3) (2010) 78-81.
- [12] L.A. Dobrzański, A. Mucha, M. Prokopiuk vel Prokopowicz, A. Drygała, K. Lukaszewicz: Arch. Mater. Sci. Eng 70(2) (2014) 70-76.
- [13] S. Ito, P. Chen, P. Comte, M.K.Nazeeruddin, P. Liska, P. Péchy, M. Grätzel: Progress in Photovoltaics: Research and Applications (in print).
- [14] K. Siuzdak: Physics in school 1 (2014) 29-32 (in Polish).
- [15] M. Zalas, B. Gierczyk, M. Klein, K. Siuzdak,

- T. Pędziński, T. Łuczak: *Polyhedron* 67(8) (2014) 381-387.
- [16] M.T. Sarniak, *The basics of photovoltaic*, Publishing House of Warsaw University of Technology, Warsaw, 2008 (*in Polish*).
- [17] K. Lukaszewicz, M. Pawlyta, I. Pasternak, L.A. Dobrzański, M. Prokopiuk, M. Prokopowicz, M. Szindler, A. Drygala, J. Sitek, *Surf. Eng.* 36(11) (2016) 816-822.
- [18] X.-D. Gao, X.-M. Li, X.-Y. Gan: Enhancing the Light Harvesting Capacity of the Photoanode Films in Dye-Sensitized Solar Cells, *Solar Cells - Research and Application Perspectives: Chapter 7*, 169-202.
- [19] M. Zhu, Xin Li, W. Liu, Y. Cui: *Journal of Power Sources* 262 (2014) 349-355.



EFFECTS OF CHEMICAL COMPOSITION ON MECHANICAL PROPERTIES OF Al-Mg-Si-Mn BASED ALLOYS

Olena Prach¹, Oleksandr Trudonoshyn², Maxim Puchnin^{3,*}

¹ Technische Universität Darmstadt, Alarich-Weiss-Straße 2, D-64287 Darmstadt, Germany

² Friedrich-Alexander-Universität Erlangen-Nürnberg, Martensstraße 5, 91058 Erlangen, Germany

³ Czech Technical University in Prague, Karlovo náměstí 13, 12135, Prague 2, Czech Republic

*corresponding author: e-mail: maxim.puchnin@fs.cvut.cz

Resume

Effects of chemical composition and heat treatment on the microstructural and mechanical properties of cast Al-Mg-Si-Mn alloys were investigated. The as-cast and heat treated alloys were investigated by microhardness, macrohardness and tensile stress measurements, scanning and transmission electron microscopy, energy dispersive X-ray analysis and differential scanning calorimetry. It was observed that the mechanical properties depend strongly on composition and addition of excess elements and eutectic phase. Heat treatment leads to the enhancement of all mechanical properties of alloys, which are the result of several mechanisms.

Article info

Article history:

Received 28 November 2016

Accepted 24 January 2017

Online 3 March 2017

Keywords:

Al-Mg-Si-Mn alloys;

Mg excess;

Si excess;

Microstructure;

Mechanical properties.

Available online: <http://fstroj.uniza.sk/journal-mi/PDF/2017/02-2017.pdf>

ISSN 1335-0803 (print version)

ISSN 1338-6174 (online version)

1. Introduction

Interest in heat treatable Al-Mg-Si aluminum alloys has been on the rise due to the ability to modify alloy hardness and thereby improve mechanical properties. The hardening effects arises as a result of interacting dislocations with the precipitates, which act as obstacles to the dislocation motion [1, 2]. It is well known that the ductility of such alloys decreases with increasing Si content and the brittle coarse Si particles usually make further deformation difficult [3].

Nevertheless, it is not only important to apply heat treatment conditions, but also to determine the optimal chemical composition of the material. The structure of Al-Mg-Si alloys consists of such phases as: solid solution of α -Al, primary Mg_2Si crystals and eutectic of Al- Mg_2Si .

An excess of Mg can decrease the solubility of Mg_2Si in the α -Al and

obviously increases strength of materials after heat treatment [4, 5]. An excess of Mg in the Al- Mg_2Si system moves the eutectic point to a lower Mg_2Si concentration. It has also been shown that excess Mg in Al- Mg_2Si alloys can promote the formation of primary Mg_2Si and show that increasing Mg content decreases the volume fraction of the α -Al matrix and increases the volume fraction of Al- Mg_2Si eutectic phase [6 - 9].

An excess of Si significantly affects the diffusion of Mg and Si in Al liquid and produces α -Al dendrite structures. Increase of Si excess in the Al- Mg_2Si -Si composites leads to an increase of the solidification range. The aspect ratio of eutectics and size of primary particles are decreased with the increase of Si content in Al- Mg_2Si composites [10]. Also, excess Si has a positive effect on the properties of alloys after heat treatment. Authors [11, 12] show positive effect with subsequent heat

treatment on tensile stress alloys with excess Si. In the works [12, 13] beneficial action after aging on hardness and microhardness as well is shown. However, simultaneous modifications of chemical composition and heat-treatment and their effect on the mechanical properties of Al-Mg-Si alloys have not yet been investigated.

The main task of the paper is to elucidate influence of chemical composition on the mechanical properties and structure of Al-Mg-Si-Mn alloys. This investigation was performed through an examination of microstructural properties, including chemical composition at the micro-scale, as well as macroscopic measurements of mechanical properties, providing an understanding of the behavior of these alloys across several length scales

2. Materials and methods

The present article follows an earlier research of Al-Mg-Si alloys [14, 15]. The chemical compositions of evaluated alloys are represented in Table 1.

All alloys were prepared in an electric resistant furnace using graphite crucibles. High purity aluminum (A99.997), AlMg50, AlSi25 and AlMn26 were used as master alloys. The melt with the temperature (720 ± 5) °C had been degassed under argon atmosphere during 10 minutes.

Two types of heat treatment were applied. The first type was a solution treatment (in an electrical resistance furnace) and quenching in water at room temperature. The second type of heat treatment is T6, which combines solution treatment at 570 °C (60 min.), quenching in water and artificial aging at 175 °C over a variety of times.

Hardness was measured by a Universal testing machine (EMCOTEST M4C 075/750) with a ball diameter of 2.5 mm and a load of 62.5 kg, time of loading was 10 sec. Microhardness tests were carried out on polished non-etched specimens on a LECO M-400-G1 microhardness tester, HV0.05 with a standard indentation time. Tensile tests were carried out using testing machine (INSTRON 5582, USA), according to the standard EN ISO 6892-1.

Samples for microstructure observations in scanning electron microscope (SEM) were prepared using conventional metallographic techniques. The composition of the phases was measured by EDX analysis using SEM (JEOL JSM-7600F High Resolution Scanning Electron Microscope with EDS analysers (Oxford INCA Energy 250, UK), Japan) with accelerating voltage of 15 kV. To minimise the influence from the interaction volume during the EDX quantification, five point analyses on selected particles were conducted for each phase and the average was taken as the measurement.

Table 1

Nominal composition of alloys, wt. % (Al – bal.).

Elements	Alloys						
	M3	MS1	MS2	M59	MS3	MS4	MS5
Mg	6.0	7.0	7.0	5.0	7.0	7.0	7.0
Si	0.4	1.0	2.0	2.0	3.0	4.0	5.0
Mn	0.6	0.6	0.6	0.6	0.6	0.6	0.6
Expected Mg ₂ Si content	1Mg ₂ Si- 5Mg	3Mg ₂ Si- 5Mg	6Mg ₂ Si- 3Mg	6Mg ₂ Si- 1Mg	9Mg ₂ Si- 1Mg	10.5Mg ₂ Si- 0.5Si	10.5Mg ₂ Si- 1.5Si

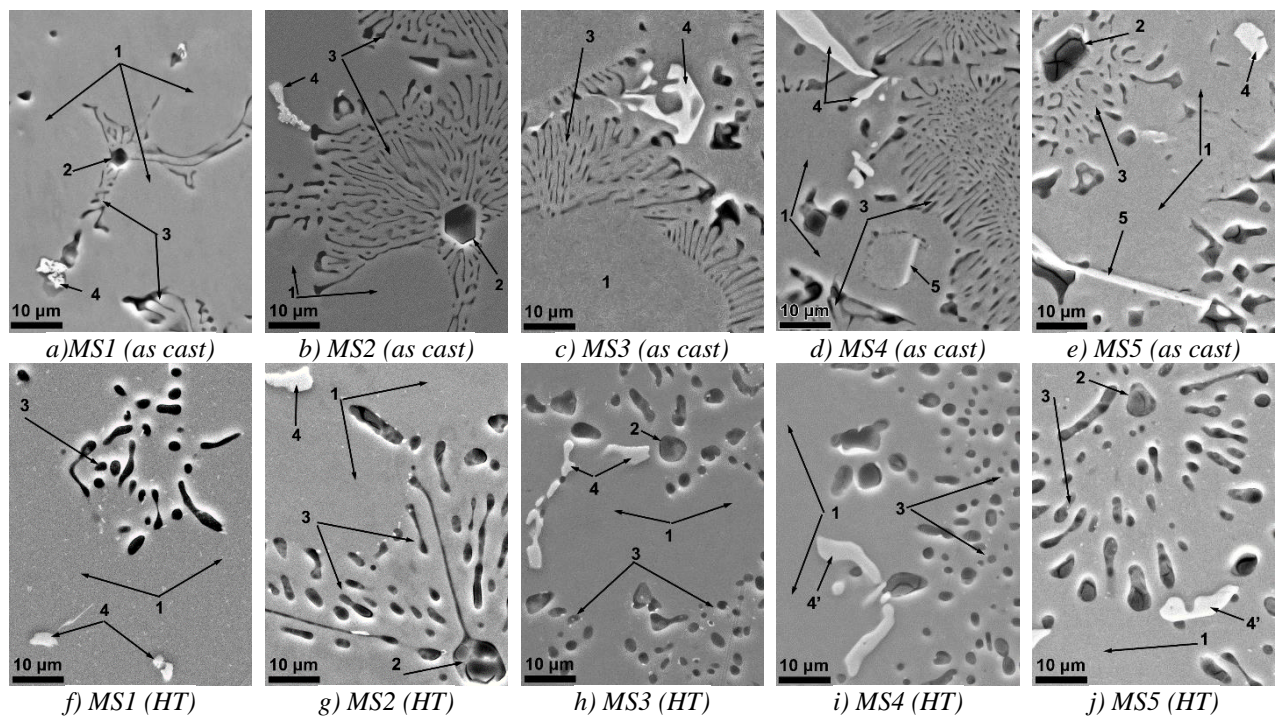


Fig. 1. Microstructure of Al-7Mg-XSi-0,6Mn alloys: a) - e) as cast, f) - j) after heat treatment.

Table 2

Average composition of α -Al solid solution in alloys measured by EDX.

Alloy	Mg/Si ratio	Chemical composition, wt. %						
		O	Mg	Al	Si	Mn	Fe	
M3	AC*	15.0	0.9	5.4	93.0	-	0.6	0.1
	HT**		0.8	5.6	92.9	-	0.	0.1
MS1	AC	7.0	0.9	4.4	94.8	0.2	0.6	0.1
	HT		0.9	5.8	92.6	0.1	0.6	-
MS2	AC	3.5	1.1	3.0	95.0	0.3	0.6	-
	HT		1.1	3.7	94.5	0.1	0.6	-
MS9	AC	2.5	0.7	1.9	96.6	0.3	0.5	-
	HT		0.6	1.9	96.7	0.3	0.5	-
MS3	AC	2.2	0.9	2.4	95.7	0.4	0.5	0.1
	HT		1.0	2.4	95.6	0.4	0.5	0.1
MS4	AC	1.8	1.1	2.0	95.9	0.5	0.5	-
	HT		0.8	0.9	97.1	0.7	0.5	-
MS5	AC	1.4	1.0	1.7	95.9	0.8	0.5	0.1
	HT		1.3	0.8	96.0	1.4	0.5	-

* - as-cast condition, ** - alloy after heat treatment

3. Results and discussion

Microstructure and elements distribution.

Fig. 1 represents the polished microstructure of samples. All alloys exhibit equiaxial grain structure. The following phases constituents can be distinguished based on the results of EDX analysis:

1. Matrix of α -Al (light areas);
2. Primary Mg_2Si crystals (black);

3. Eutectic of Al- Mg_2Si (dark-grey areas);
4. Manganese phases $Al_6(Mn,Fe)$, $\alpha-Al_{15}(Mn,Fe)_3Si_2$;
- 4'. Mangan-silicon phase $\beta-Al_5(Mn,Fe)Si_2$;
5. Silicon-manganese phase $\delta-Al_4Si_2(Mn,Fe)$;

In the present series of alloys, Mg and Si content in solid solution changes with alteration of the Mg/Si ratio in alloys (Table 2). Mg is considered in excess when the ratio is more than 2, and excess of Si - less than 2. For all

alloys Mn content in α -Al solid solution is 0.5 - 0.6 wt. % (Table 2). Existence of an insignificant peak of oxygen in EDX-spectrum is explained by tendency of Al and Mg_2Si to oxidation. The average composition of α -Al matrix for all samples is represented in Table 2.

Homogenization equalizes the distribution of all elements in the grain and increases the excess element (Mg or Si) in α -Al matrix (Table 2). Exceptions are M59 and MS3 alloys, in which the concentration of the Mg and Si in solid solution changes slightly. It can depend on Mg/Si ratio, which is close to stoichiometric in these alloys.

Mn- and Si-containing phases. Due to the presence of iron in the Mn ligature which have poor solubility in Al-Mg-Si alloys, we observe the formation of acicular-shaped intermetallic inclusions of high Fe and Si content, which reduce the strength and ductility of the alloys. To neutralize the negative effect of the Fe-containing phase [12 - 16], investigated alloys are additionally doped by 0.6 % Mn.

In alloy with the nominal composition of Al-7Mg-5Si wt. %, two eutectics (Al- Mg_2Si and Al-Si) are formed [12]. However, the eutectic Al-Si was not detected in the alloy with a nominal composition Al₇Mg₅SiMn (Fig. 1 j and 4 d). Therefore an excess of silicon with manganese and iron form several types of manganese phase in submitted alloys.

As it is shown by further studies, the addition of 0.6 wt. % of manganese in the alloy with nominal composition Al-7Mg-3Si improves its mechanical properties. Thus tensile strength and yield strength of the alloy with manganese addition increases on average by 30 %.

The morphology of primary Mn-containing phase observed in all alloys is shown in Fig. 1. Its chemical composition and stoichiometry are represented in Table 3. These phases can be identified as Al₆(Mn,Fe),

α -Al₁₅(Mn,Fe)₃Si₂, β -Al₅(Mn,Fe)Si, δ -Al₄(Mn,Fe)Si₂. As it can be seen from Fig. 1 and Table 3, heat treatment promotes the transformation of metastable phases to stable conditions [16 - 18].

Eutectic. An overview of the thermal effects in the investigated alloys and therefore their melting point can be obtained from the DSC curves. The experiments were conducted in alloys with different Mg and Si content. Fig. 2a shows the curves of the changes in the heat flow depending on the temperature for the MS2, M59 and MS3 alloys. In the temperature range from 20 - 590 °C no thermal effects were observed. When the temperature reaches close to 590 °C on the all of heating curve, a negative thermal effect occurs, which corresponds to an endothermic reaction. The first endothermic effect can be attributed to the melting of the eutectic (Al) + (Mg_2Si) and starts at $T = 594 \pm 3$ °C. The second heat effect corresponds to the melting of α -Al matrix. As it can be seen, amount of the eutectic (Al) + (Mg_2Si) as well as excess of Mg does not significantly effect on the behavior of alloys during heating. Peaks corresponding to the melting of Mn-containing phases have not been detected due to a small amount. Therefore, we can judge, that the initial melting point of alloys of Al-Mg-Si is the melting point of (Al) + (Mg_2Si) eutectic - 594 °C.

Another situation occurs in alloys with excess of Si that can be seen on Fig. 2b. In MS4 and MS5 alloys, in comparison with other studied alloys, new peaks were detected. They start close to 570 °C and merge with the peak of (Al) + (Mg_2Si) eutectic. Due to [17, 18] they can be classified as a melting of Mn- and Si- containing phases. Thus, α -(AlFeSi) and β -(AlMnFeSi) phases have melting points in range 560-570 °C, (Al)-(Si) eutectic - 575 °C and δ -(AlMnFeSi) - 596 °C. The temperatures of these reactions are close to each other and to identify them on the DSC curves it is necessary to use more precise equipment.

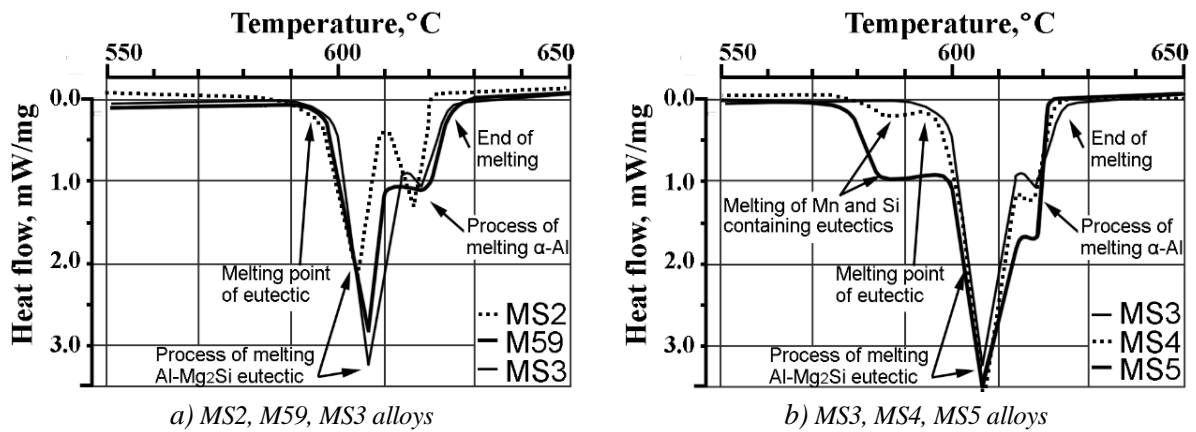


Fig. 2. Comparison DSC curves of MS2, M59, MS3 (a) and MS3, MS4, MS5 (b) alloys (cooling rate 10 K/min).

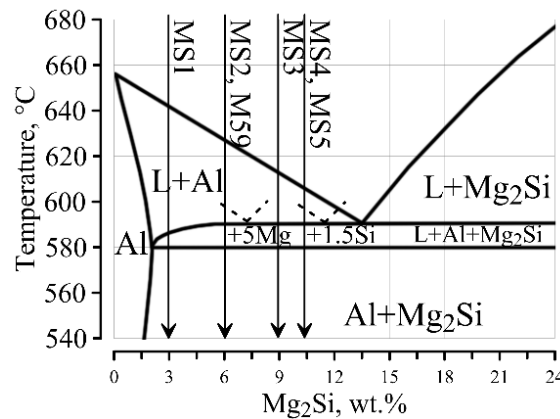


Fig. 3. Equilibrium phase diagrams of Al-Mg₂Si system.

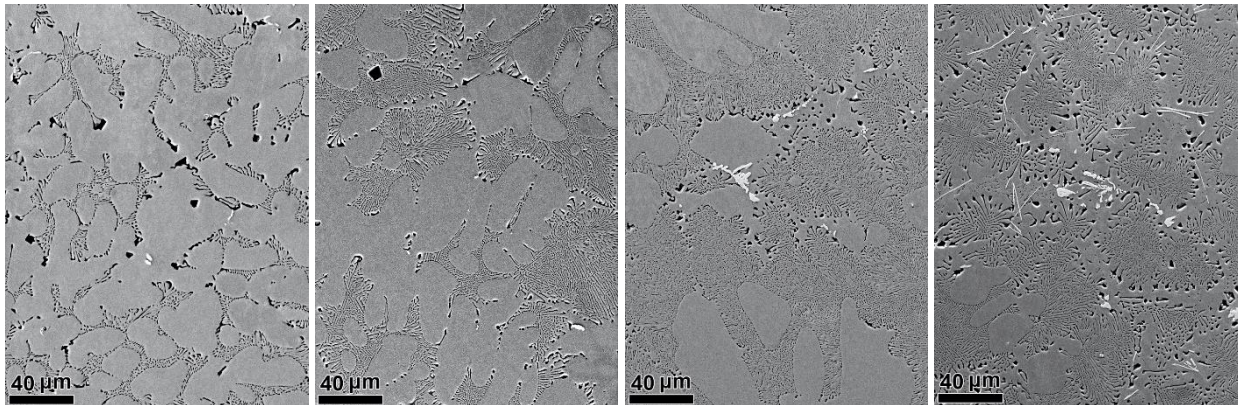


Fig. 5. Volume fraction of Al-Mg₂Si eutectic in: a) M59 alloy, b) MS2 alloy, c) MS4 alloy, d) MS5 alloy dependency on Mg and Si content.

With the addition of Mg into the Al-Mg₂Si system, the eutectic point moves towards the corner with lower Mg₂Si concentration (Fig. 3), the volume of primary α -Al decreases with increasing of the Al-Mg₂Si eutectic volume (Fig. 4 a, b). As it was mentioned in [21], the Al-Mg₂Si eutectic volume fraction grows with the increase of Mg₂Si in the Al-Mg₂Si

alloys.

Increase of excess of Si in the Al-Mg₂Si alloys leads the eutectic point to higher Al concentration and decrease of the volume of primary α -Al and increase of the Al-Mg₂Si eutectic volume. In MS5 alloy with 1.5 wt. % excess of Si, primary α -Al practically disappears, and the volume fraction of Al-Mg₂Si

eutectic reaches maximum (Fig. 4 c,d).

Mechanical properties. The results of hardness and tensile tests are summarized in Fig. 5. As the result of solution treatment both macrohardness (HB) and microhardness (HV0.05) values are significantly decreasing (except MS5 alloy). Artificial aging leads to an increase in all mechanical properties of the investigated alloys. Changing during heat treatment is the result of several processes, which simultaneously occurs during heating.

The first process is the eutectic spheroidization. The higher solution treatment temperature leads to faster eutectic lamella decomposition into smaller segments and

to a spheroidizing effect [15]. This process (according to the results as presented on Fig. 5) leads to a decrease in the hardness of the alloys.

The second process is dissolution of primary Mn-containing phases and the formation of dispersoids, which include Mn, Si and Fe. These particles can be identified as α -(Al₁₅(Mn,Fe)₃Si₂) phase [21, 22]. Absence of coherence of phase α -(Al₁₅(Mn,Fe)₃Si₂) with α -Al probably affects the decrease of the hardness of the alloys, (along with disintegration of eutectic cells). Also, the dissolution of the β' -Mg₉Si₅ particles occurs during homogenization.

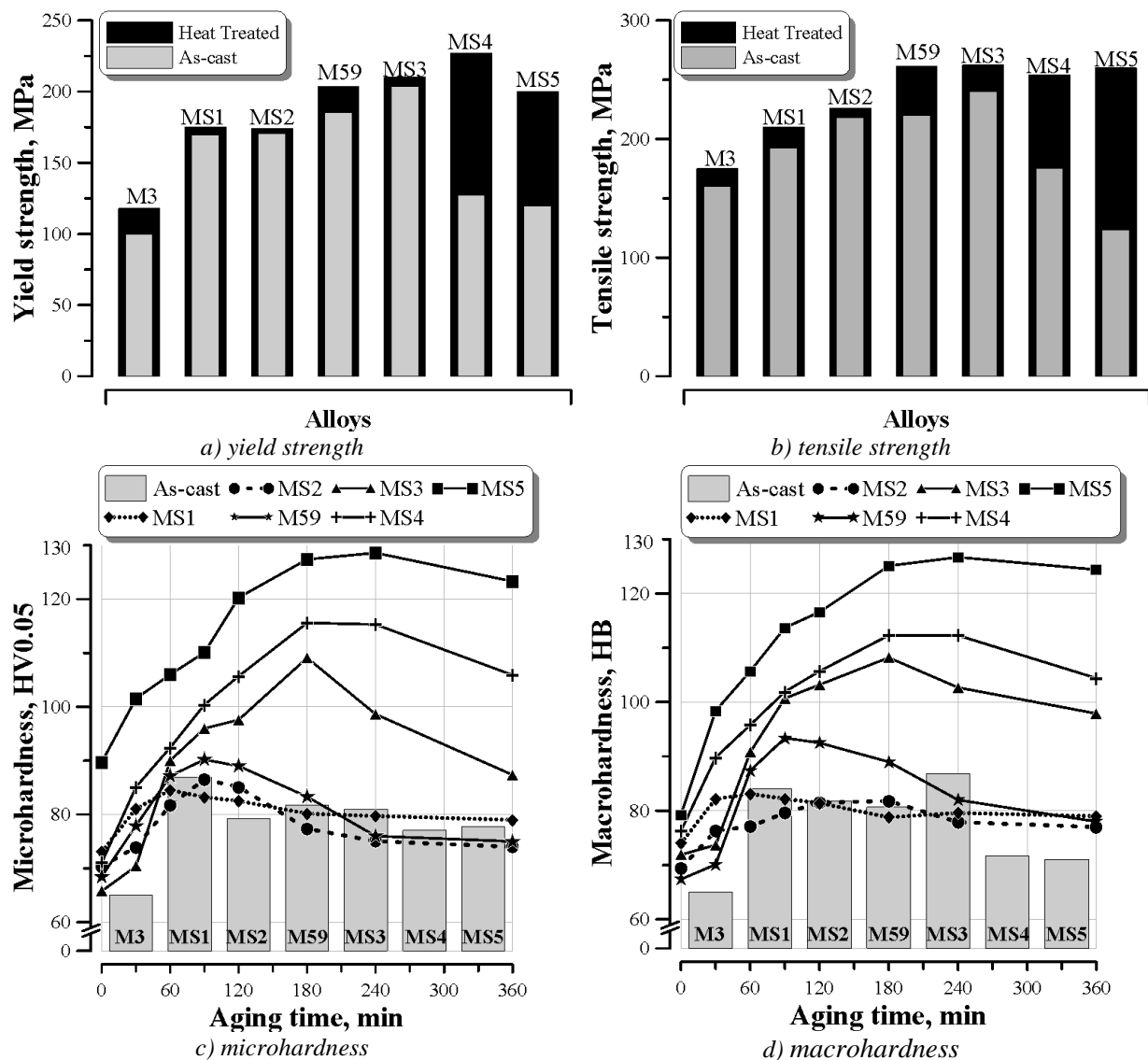


Fig. 5. Mechanical properties of MS-series.

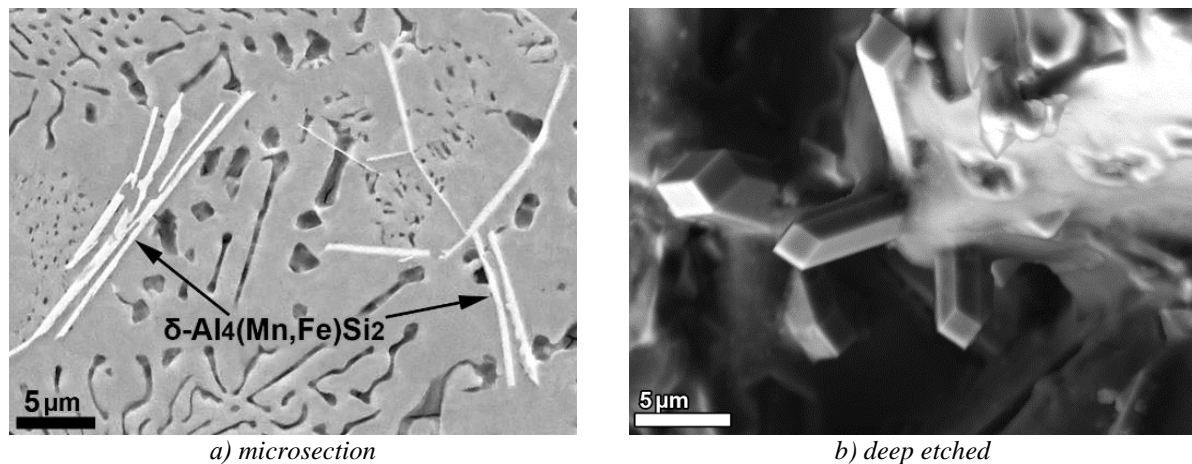


Fig. 6. Morphology of needle-shaped polyhedral δ -Al₄(Mn,Fe)Si₂ phase in MS5 alloy.

Table 3

Average composition of Mn-containing phases measured by EDX.

Phase name	Alloy	Chemical composition, wt.%						
		O	Mg	Al	Si	Mn	Fe	Cu
$\text{Al}_6(\text{Mn,Fe})$ (blocky-shaped)	M3	1.4	0.8	73.2	0.1	16.1	8.3	0.1
	MS1	1.6	1.8	70.7	1.1	16.2	8.5	0.1
	MS2 (AC)	2.1	2.2	70.4	1.0	16.4	7.8	0.1
α -Al ₁₅ (Mn,Fe) ₃ Si ₂ , (blocky-shaped, stable phases)	MS2 (HT)	0.9	0.6	65.6	5.5	17.8	9.4	0.2
	M59 (AC)	1.8	0.9	70.5	5.5	13.2	7.8	0.3
	M59 (HT)	1.0	1.1	70.7	5.8	13.5	7.5	0.4
	MS3 (AC)	1.7	0.7	66.5	4.9	14.3	11.3	0.6
δ -Al ₄ (Mn,Fe)Si ₂ (acicular-shaped)	MS3 (HT)	1.5	0.7	69.7	4.8	13.3	9.9	0.1
	MS4 (AC)	1.5	1.1	60.4	26.8	7.6	2.2	0.4
β -Al ₅ (Mn,Fe)Si (blocky-shaped, stable phase)	MS5 (AC)	1.1	0.7	58.1	21.3	16.8	1.7	0.3
	MS5 (AC)	0.5	0.2	59.2	11.9	25.1	2.4	0.7
	MS4 (AC)	0.8	0.6	62.0	10.4	21.8	4.0	0.4
	MS4, MS5 (HT)	1.6	1.00	63.5	11.6	21.9	2.3	0.1

The last process occurs in alloy MS4, MS5 is transformation of metastable acicular-shaped δ -phases (Fig. 6) to more stable state due to the diffusion processes [23, 24]. After solution treatment the excess of Si from the δ -phase dissolves in α -aluminum solid solution (Tables 2, 3). As it can be seen from Fig. 6c this process is confirmed by the results from microhardness tests.

Hardness and tensile strength of the cast Al-Mg₂Si alloys do not increase with the growth of Mg content (MS2 and M – alloys with same volume of Mg₂Si and different values of Mg), but can relate to the size and morphology of the eutectic and primary Mg₂Si phases (M3 and MS1, M59 and MS3 – alloys with same

the value of Mg and different volume of Mg₂Si), it can be seen from Fig. 5. Similar results were obtained in the works [6, 11].

The alloys of Al-Si-Mg system with increase of Mg content up to a certain quantity leads to increase of mechanical properties, but further increase of the Mg content leads to decrease of mechanical properties [25]. As can be seen from the graphs (Fig. 5), heat treatment does not affect on the mechanical properties (both of hardness and tensile strength) of alloys with extra magnesium. Also, heat treatment of alloys with extra silicon improves the mechanical properties. With increasing time of artificial aging (at 175 °C) the hardness of alloys with extra silicon grows.

It can be explained by a sufficient amount of silicon in solid solution to form a larger number of strengthening particles.

Fractography analysis. Insignificant hardening effect on alloys with extra magnesium content was confirmed by results of fractography analysis. Behavior of the fracture surface also confirms that the main strengthening phase in the studied system is the Al-Mg₂Si eutectic. With increase of the eutectic amount the percentage of brittle surfaces proportional increases, thereby tensile strength become higher (from the quasi-viscous MS1 to transgranular MS3).

Initiation of destruction is on the line of the eutectic cells – α -matrix grains and eutectic cells – eutectic cells (alloys MS1, MS2, MS3). Additional stress concentrations

(in alloys MS4 and MS5) are caused by the presence of elongated acicular-shaped inclusions (δ -phase). This confirms our assumption that the cause of the sharp deterioration of mechanical properties in the as-cast state is silicon-containing particles. The dendrites of α -matrix behave similar to grains and strong interaction between inclusions and slip bands, which generates at the grain boundaries during the plastic deformation process [26]. The final fracture paths tend to pass through the eutectic cells and the fracture of eutectic generates the formation of flat areas (Fig. 7). The fracture path preferentially goes through the shrinkage porosity in the case of the existence of excessive shrinkage defects, which results in the significant decrease of mechanical properties [27].

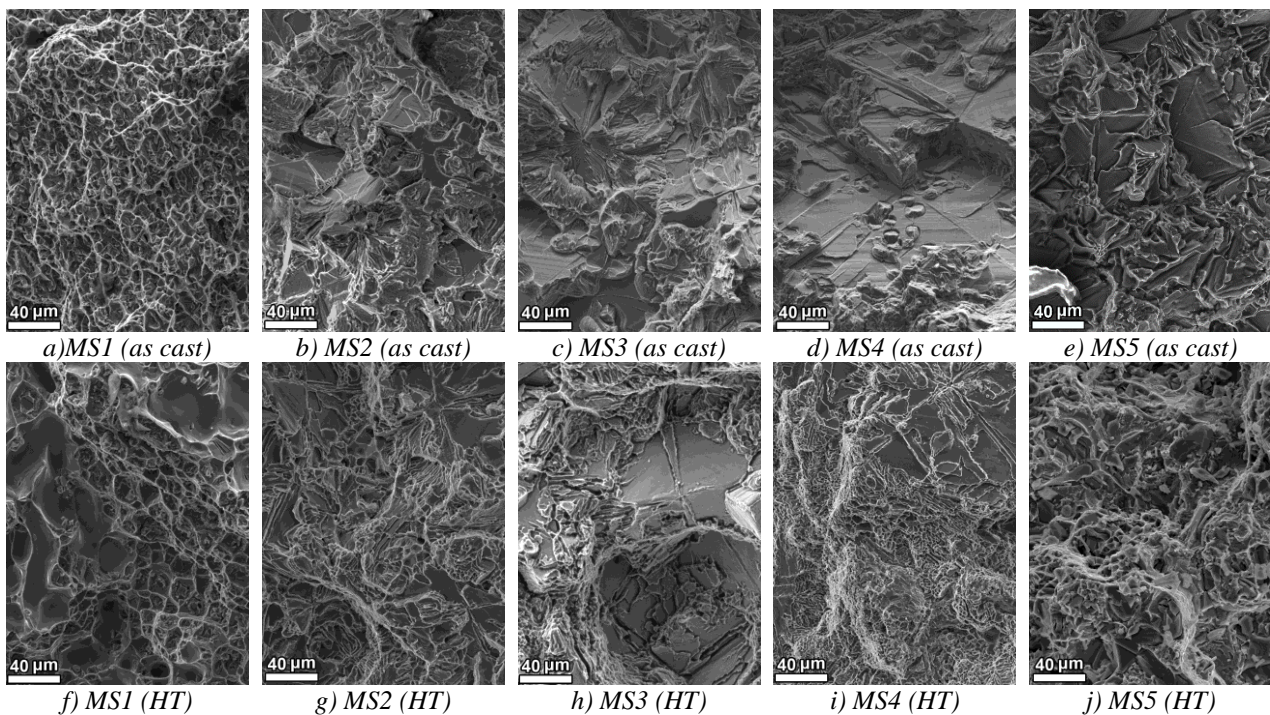


Fig. 7. Fractography of Al-7Mg-XSi-0,6Mn alloys: a) - e) as cast, f) - j) after heat treatment.

Solution treatment leads to the quantity reduction of brittle surfaces compared with the cast condition and the formation of a viscous fracture. This is associated with spheroidization of the eutectic lamellas. It confirms decrease of mechanical properties that we can see on the graphs of hardness. Similar effect of heat

treatment on the formation of the fracture surface was obtained by the author [27].

4. Conclusions

Increase of Si content leads to the formation of less stable phases. In alloys with an excess of Si metastable δ -Al₄(Mn,Fe)Si₂ phases are

formed. This leads to the degradation of mechanical properties. It has been found that the an excess of silicon (MS4 and MS5 alloys) promote the formation of strengthening particles in α -matrix during aging, which leads to appreciable increase of tensile strength.

The higher solution treatment temperature leads to faster eutectic lamella decomposition into smaller segments and to spheroidizing effect.

Homogenization equalizes distribution of all elements in grain and increases the excess element (Mg or Si) in α -Al matrix and transformation of metastable silicon-manganese acicular-shaped δ -phase to more stable state (α or β) due to diffusion processes.

Excess magnesium did not have a meaningful effect on the mechanical properties of alloys.

The main strengthening phase in the studded system is the eutectic cells of Al-Mg₂Si.

Acknowledgements

The authors thank our colleagues Prof. K. Mykhalenkov and V. Boyko for the provision of alloys for research and participation in discussions, although they may not agree with all of the conclusions of this paper. The authors also thank the Chair Metallic Materials TU-Berlin, where alloys for this study were melted.

This research was supported by the Visegrad Fund (V4EaP) and the German Academic Exchange Service (DAAD).

This work was supported by the Ministry of Education, Youth and Sport of the Czech Republic, program NPUI, project No LO1207.

References

- [1] N. Fridlyander, V.G. Sister, O.E. Grushko, V.V. Berstenev, L.M. Sheveleva, L.A. Ivanova: Metal Science and Heat Treatment 44(9) (2002) 365-370.
- [2] S. Zajac, B. Bengtsson, C. Jonsson: Mater. Sci. Forum 396-402 (2002) 399-404.
- [3] Y. Wang, H. Liao, Y. Wu, J. Yang: Materials and Design 53 (2014) 634-638.
- [4] C. Li, Y. Wu, H. Li, X. Liu: Journal of Alloys and Compounds 477 (2009) 212-216.
- [5] J. Zhang, Z. Fan, Y. Q. Wang, B. L. Zhou: Mater. Sci. Technol. 17 (2001) 494-496.
- [6] F. Yan, S. Jib, Z. Fanc: Mater. Sci. Forum 765 (2013) 64-68.
- [7] A. Furihata, K. Matsuda, J. Nakamura, S. Ikeno, Y. Uetani: Mater. Sci. Forum 519-521 (2006) 507-510.
- [8] A. Radziszewska: Journal of Microscopy 237(3) (2010) 384-387.
- [9] K. Matsuda, T. Yoshida, T. Wada, A. Yoshida, U. Uetani, T. Sato, A. Kamio, S. Ikeno: J. Japan Inst. Metals 62 (1998) 718-726.
- [10] J. Zhang, Y. Wang, B. Yang: J. Mater. Res. 14(1) (1999) 68-74.
- [11] J. Qingxiu, Z. Caixia, H. Xiaodong: China Foundry 6(2) (2009) 133-136.
- [12] E. Georgatis, A. Lekatou, A.E. Karantzalis, H. Petropoulos, S. Katsamakis, A. Poulia: J. Mater. Eng. Perform. 22(3) (2013) 729-741.
- [13] L. C. Doan, K. Nakai, Y. Matsuura, S. Kobayashi, Y. Ohmori: Materials Transactions, 43(6) (2002) 1371-1380.
- [14] M. Puchnin, O. Trudonoshyn, O. Prach: Mater. Tehnol. 50(2) (2016) 247-252.
- [15] O. Trudonoshyn, M. Puchnin, O. Prach: Mater. Tehnol. 50(3) (2016) 427-431.
- [16] Z. Zhihao, M. Yi, C. Jianzhong: China Foundry 9(4) (2012) 349-355.
- [17] L. Lia, R. Zhoua, D. Lua, Y. Jianga, R. Zhoua: Materials Research 17(2) (2014) 511-517.
- [18] C. Phongphisutthinan, H. Tezuka, T. Sato: Materials Transactions 52(5) (2011) 834-841.
- [19] L.F. Mondolfo. Aluminium Alloys: Structure and Properties. Butterworth & Co Publishers Ltd; 2nd Revised edition, December 1979.
- [20] N. A. Belov, D.G. Eskin, A.A. Aksenov. Multicomponent phase diagrams: applications for commercial aluminum alloys. Elsevier, 2005.
- [21] S. Otarawanna, C.M. Gourlay, H.I. Laukli, A.K. Dahle: Metallurgical And Materials Transactions A 40A (2009) 1645-1659.
- [22] L. Lodgaard, N. Ryum: Mater. Sci. Eng. A283

- (2000) 144–152.
- [23] G.A. Edwards, K. Stiller, G.L. Dunlop, M.J. Couper: *Acta Mater.* 46(11) (1998) 3893-3904.
- [24] C. Ravi, C. Wolverson: *Acta Mater.* 52 (2004) 4213–4227.
- [25] L. Hong, S. Wen-Ju, Z. Gang, L. Chun-Ming, Z. Liang: *Trans. Nonferrous Met. Soc. China* 15(1) (2005) 30-31.
- [26] J. Wen-Ming, F. Zi-Tian, L. De-Jun, Microstructure: *Trans. Nonferrous Met. Soc. China* 22 (2012) 7–13.
- [27] G. Mrówka-Nowotnik: *Archives of Materials Science and Engineering* 46(2) (2010) 98-107.

ZnO THIN FILMS PREPARED BY ATOMIC LAYER DEPOSITION

Paulina Boryło^{1,*}, Krzysztof Lukaszkoicz¹

¹ Institute of Engineering Materials and Biomaterials, Faculty of Mechanical Engineering, Silesian University of Technology, Konarskiego 18A, 44-100 Gliwice, Poland

*corresponding author: e-mail: paulina.borylo@polsl.pl

Resume

The purpose of this paper is present the influence of deposition conditions of nanometric zinc oxide thin films using atomic layer deposition on the mechanical and optical properties. The influence of the deposition temperature and the number of cycles on the transparency and adhesion of the ZnO, thin films was investigated. In addition, the results of chemical and phase composition analysis of the layers and their topography and structure were discussed. As a substrate for the investigated thin films was used glass. For the preparation of ZnO thin films was used ALD method. Selecting this method is justified by the high quality and good properties of the deposited layers.

Article info

Article history:

Received 26 September 2016

Accepted 31 December 2016

Online 3 March 2017

Keywords:

Low ZnO;

ALD;

SEM;

TEM;

UV-VIS;

Scratch test.

Available online: <http://fstroj.uniza.sk/journal-mi/PDF/2016/03-2017.pdf>

ISSN 1335-0803 (print version)

ISSN 1338-6174 (online version)

1. Introduction

Zinc oxide belongs to the semiconductor group II-IV type. It is characterized by a wide energy gap of 3.37 eV (at room temperature). Such a wide energy gap makes ZnO completely transparent to the electromagnetic spectrum of visible light. It allows using of ZnO as the transparent conductive layers (TCL). The most commonly used material for such a coating is indium-tin-oxide (ITO). However, due to the high costs of production of ITO, which are mainly generated by the high price of indium, they are sought alternative materials [1 - 5].

Today there are many methods of producing nanometric ZnO conductive layers. One promising method seems to be the atomic layers deposition method - ALD. The main advantages of this method are self-limited growth mechanism and the pulsed nature of the process. The self-limited growth mechanism makes possible to control the thickness of the deposited layer at the nanometer level. Theoretically, during

one cycle of the ALD deposited layer obtained a thickness of approx. 0.1 nm. Whereas, pulsed nature of the process allows to use more reactive precursors than is the case in the CVD process.

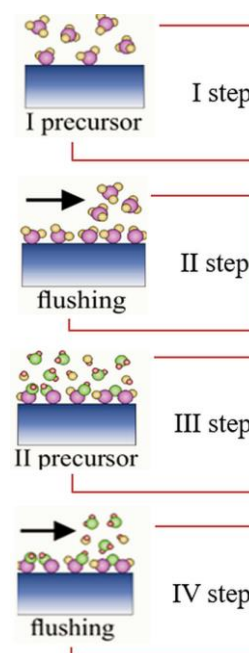


Fig. 1. Schema of the atomic layer deposition process. (full colour version available online)

Fig. 1 shows the schema of ALD process. The thin films were deposited by ALD technique are characterized by high homogeneity and conformality [4 - 10]. This article is a continuation of the tests described in [11].

2. Experimental details

Zinc oxide layer was deposited using ALD method in reactor R-200 from Picosan. As a precursor for zinc was used diethylzinc (DEZ), for oxide was deionized water (H₂O) and nitrogen (N₂) as an inert gas. The dosing time of each precursor was 0.1 s the flushing time was 4 s for DEZ and 5 s for H₂O. The process temperature was 100 to 300° C, depending on the process, and the number of cycles was 200 - 600. ZnO thin films were deposited on a glass substrate and copper ring with a carbon membrane (for transmission electron microscope).

Surface topography and microstructure were observed in a scanning electron microscope Supra 35 from Zeiss and transmission electron microscope Titan 80-300 from FEI.

The chemical composition was checked using energy dispersive X-ray spectroscopy method by Trident XM4 system from EDAX which is part of scanning electron microscope Supra 35 from Zeiss.

X-ray phase analysis was tested by X'Pert Pro diffractometer from Panalytical with a cobalt lamp.

Adhesion was tested using scratch test on the open platform equipped with a Micro-Combi-Tester from CSM. In order to scratch the sample was used a diamond penetrator in the shape of a cone. To evaluate the adhesion of the tested samples was used recording acoustic emission, frictional force and friction coefficient. Scratches were also assessed visually by optical microscopy, which is an integral part of the platform. Measurements were made according with PN-EN 1071-3. The test parameters:

- loading force: 0.03 ÷ 30 N (gradually increasing);

- loading speed: 100 N/min;
- moving speed of table: 10 mm/min;
- length of the scratch: ~3 mm.

Measurements of transparency for ZnO thin films were carried out on a UV-VIS spectrometer Evolution 220 from Thermo Scientific. The test was performed for the wavelength of visible light.

3. Results and discussion

The morphology of the surface of ZnO thin films (Fig. 2) deposited on a glass substrate by ALD is characterized by homogeneity and a nanocrystalline structure. This is confirmed by research carried out using a transmission electron microscope. The thickness of the ZnO thin film is in the range 75 -95 nm depending on the process temperature (Fig. 3).

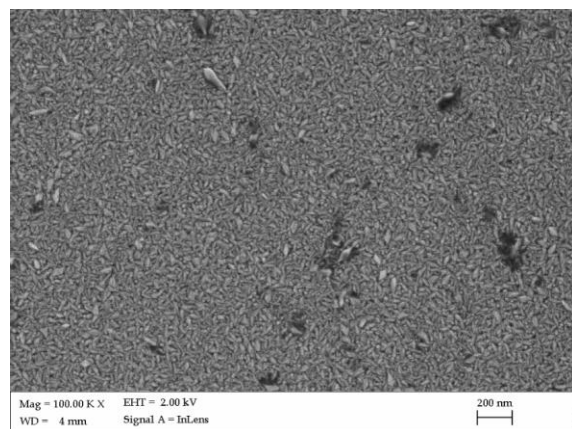


Fig. 2. SEM image of the surface topography ZnO thin film deposited on the glass substrate at 150°C. (full colour version available online)

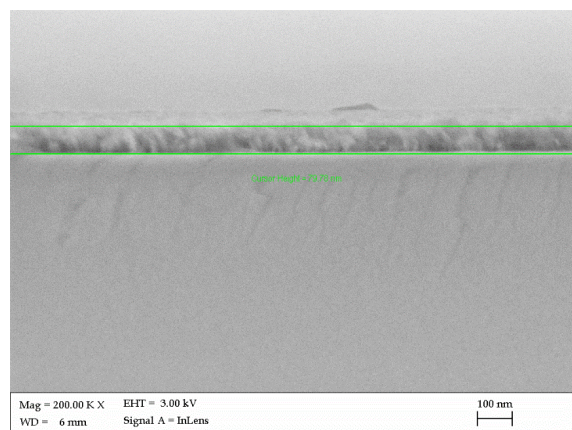


Fig. 3. SEM image of the surface topography ZnO thin film deposited on the glass substrate at 150°C. (full colour version available online)

Subsequently, for the coating's structure characterization, the TEM microscopes was used. The images presented in Fig. 4 were obtained from selected regions. The bright-field image (Fig. 4a) and dark-field image (Fig. 4b) shows a nanocrystalline character of ZnO films.

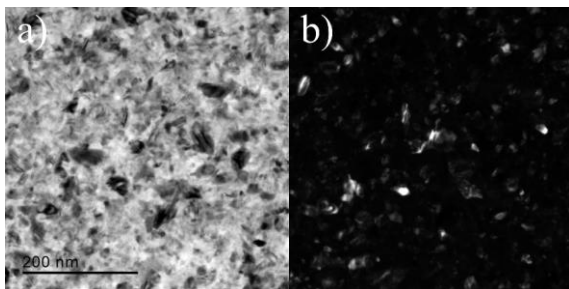


Fig. 4. TEM image of the nanostructured ZnO thin film deposited on a copper ring with a carbon membrane at 150°C; a) bright field image; b) dark field image.

In order to identify the chemical composition of the deposited thin layers was performed by EDS method. In Fig. 5 shows the EDS spectrum, which confirms the presence of the analyzed coating both zinc (characteristic peaks: 1.012 keV, 8.637 keV and 9.570 keV) and oxygen (0.532 keV). The visible spectrum

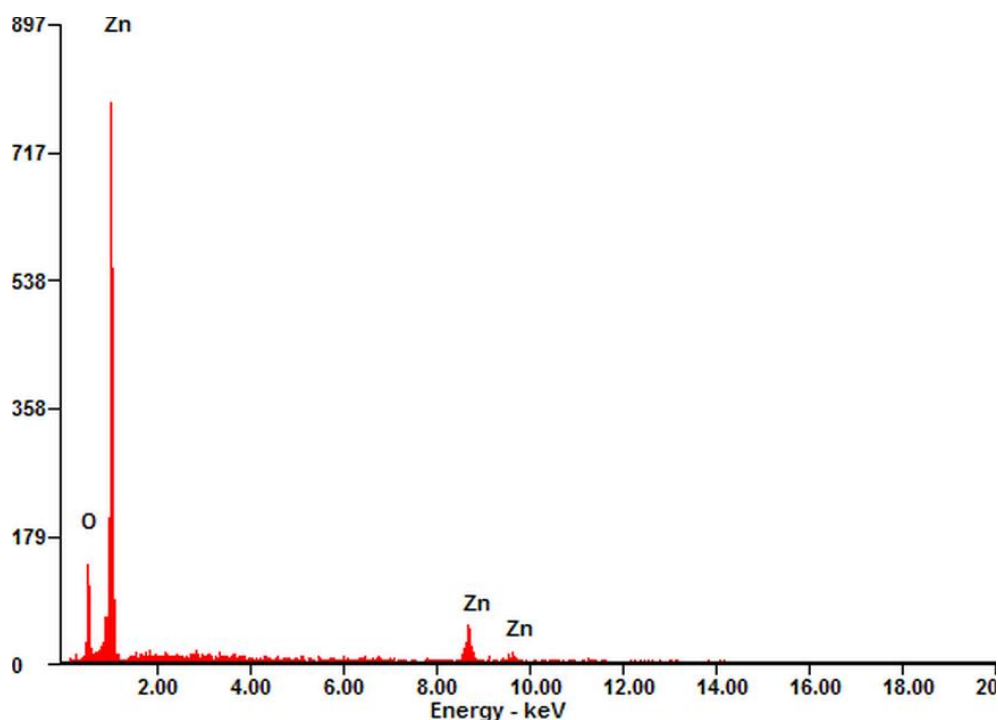


Fig. 5. EDS spectrum of the ZnO coating deposited on glass at 250°C. (full colour version available online)

is only the peaks characteristic of the coating material. The peaks of the substrate material have not been registered because the electron excitation area covered only thin film.

In Fig. 6 are shown the results of X-ray phase analysis obtained by Bragg-Brentano. The results obtained confirm the presence of ZnO phase in the thin film, because occurred the peaks characteristic of this material: 37.061° with index (010), 40.158° (002), 42.349° (011) and 66.798° (110). The peaks were identified using JCPDS files.

To study the adhesion of coated layers scratch test was used. The results are shown in Table 1, Fig. 7. Based on the results, the obtained values for each sample are very close to each other. Also in the case of critical value - LC1 (Table 1), which is a critical parameter of adhesion. Differences between the values for the individual samples are very low. On this basis, it can be concluded that the temperature deposition process of ZnO thin films by ALD method does not have a significant impact on the ZnO thin films adhesion to the substrate made of glass.

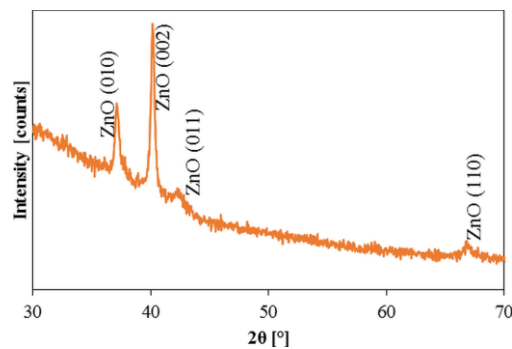


Fig. 6. X-ray diffractometer ZnO thin film deposited on the glass obtained by Bragg-Brentano, the process temperature was 150 °C and number of cycles was 750.
(full colour version available online)

Table 1.

The results of the scratch test of ZnO thin films deposited at a temperature of 100-300°C, 600 cycles.

Sample	Value of indenter load F_n (N)		
	L_{c1}	L_{c2}	L_{c3}
100	3.62	7.87	23.5
150	2.88	7.96	25.2
200	2.50	7.94	25.2
250	2.37	8.09	24.8
300	2.33	7.97	21.6

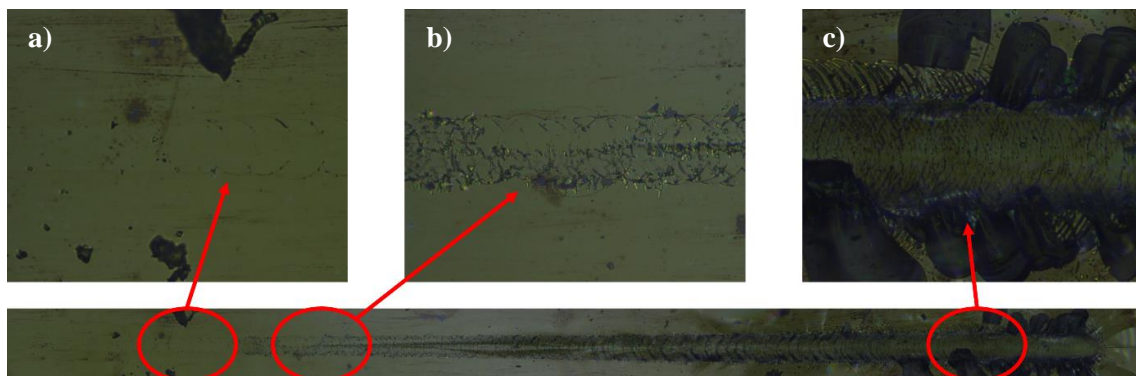


Fig. 7. Types of damage caused during the scratch test: a) the type of Hertz circular cracks (L_{c1} was 4.06 N), b) cracks inside the trace scratches (L_{c2} was 7.68 N), c) cohesive chipping along the edges and inside scratches (L_{c3} was 23.80 N), ZnO thin films deposited at a temperature of 100°C at a number of cycles of 600.
(full colour version available online)

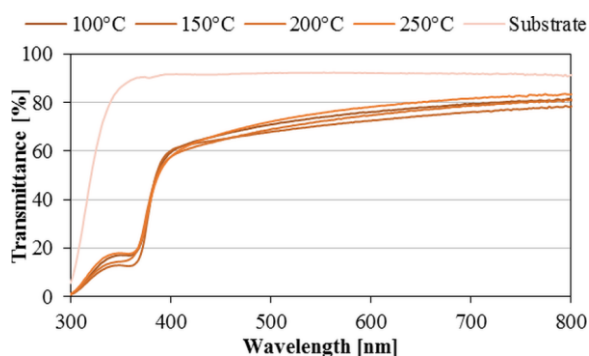


Fig. 8. The results of the measurement of transparency for ZnO thin films deposited at a temperature of 100-250°C at a constant number of cycles of 300.
(full colour version available online)

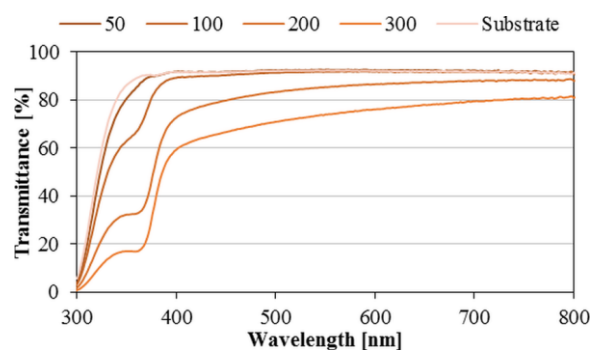


Fig. 9. The results of the measurement of transparency for ZnO thin films deposited at 100°C with the number of times the range of 50-300.
(full colour version available online)

Fig. 8 and 9 shows results of measurements of the transparency of ZnO thin films deposited on the glass substrate depending on the process temperature and the number of cycles. The results were compared with results of the measurement of transparency for a glass substrate. From the obtained results it can be concluded that the deposition temperature has no significant effect on the transparency of the coatings tested (Fig. 8). However, the number of cycles has a significant impact on transparency. If the number of cycles is greater, the thicker layers are deposited and thus lower transparency of produced layers is achieved (Fig. 9).

4. Conclusions

Surface topography and microstructure shows that thin films deposited by ALD are nanocrystalline, homogeneous and uniformity.

Analysis of the chemical composition and phase confirmed the presence of ZnO layers on the surface of the investigated material and showed no evidence of contamination.

Scratch test of ZnO thin film into a glass substrate showed that the temperature of the ALD process hasn't significant effect for adhesion value.

Also, the temperature of the process does not effect on the transparency of thin films investigated. In contrast, the number of ALD cycles, and as a result thickness of ZnO thin films, significantly affects the level of transparency. In addition, all test samples

showed a sharp decline in transparency for the near infrared (below 400 nm).

Acknowledgements

The project was funded by the National Science Centre on the basis of the contract No. DEC-2013/09/B/ST8/02943.

References

- [1] R. Escudero, R. Escamilla: Solid State Communications 151(2) (2011) 97–101.
- [2] T. Tynell, M. Karppinen: Semicond. Sci. Tech. 29 (2014) 043001.
- [3] Zs. Baji, Z. Lábadi, Gy. Molnár, B. Pécz, K. Vad, Z.E. Horváth, P.J. Szabó, T. Nagata, J. Volk: Thin Solid Films 562 (2014) 485–489.
- [4] J. Laube, D. Nübling, H. Beh, S. Gutsch, D. Hiller, M. Zacharias: Thin Solid Films 603 (2016) 377-381.
- [5] J. L. Tian, H. Y. Zhang, G. G. Wang, X. Z. Wang, R. Sun, L. Jin, J. C. Han: Superlattices and Microstructures 83 (2015) 719-729.
- [6] L.A. Dobrzański, M. Szindler: J. Achiev. Mater. Manuf. Eng. 59(1) (2013) 13-19.
- [7] S.M. George: Chem. Rev. 110 (2010) 111-131.
- [8] N. Pinna, M. Knez: Atomic Layer Deposition of Nanostructured Materials, Wiley-VCH, Weinheim, 2012.
- [9] A. Pakkala, M. Putkonen: In: Handbook of deposition technologies for films and coatings - science, applications and technology, Ed.: P. M. Martin, Elsevier Inc., USA, 2010, pp. 364-391.
- [10] R. L. Puurunen: J. Appl. Phys. 97 (2005) 121301.
- [11] P. Boryło, K. Lukaszkwicz, M. Szindler, M. Basiaga: J. Achiev. Mater. Manuf. Eng. 73(2) (2015) 86-91.



WELDING OF THE TUBE GIRDER COVER MADE OF THE C-Mn STEEL

Vukić Lazić¹, Dušan Arsić¹, Ružica Radoslava Nikolić^{1,2,*},
Srbislav Aleksandrović¹, Milan Djordjević¹, Branislav Hadzima²

¹ Faculty of Engineering, University of Kragujevac, Sestre Janjić 6, 34000 Kragujevac, Serbia

² Research Center, University of Žilina, Univerzitna 1, 010 26 Žilina, Slovak Republic

*corresponding author: e-mail: ruzicarnikolic@yahoo.com

Resume

The welding procedure and technology for welding the cover of the tube girder is presented in this paper. The tube cover is made of the C-Mn steel. The welding has to be performed over the whole perimeter in the V groove. Since the structure in question is a very responsible one (a part of the assembly of the large hadron collider – LHC), the check of the base metal chemical composition and the mechanical properties had to be conducted before actual prescribing of the welding process type and the complete welding technology. Then the weldability of the base metal was estimated, which showed that this particular steel was conditionally weldable with application of preheating. The welding technology was prescribed, based on the previously determined parameters including the welding procedure and the filler metals selection. The prescribed technology was afterwards executed on the selected experimental samples. To verify that the selected technology was adequate, the hardness and the microstructure of all the zones of the welded joints were determined. Analysis of executed experimental welds on chosen samples has confirmed that the welding technology was appropriate and that it could be applied to the real part – the LHC assembly.

Article info

Article history:

Received 05 December 2016

Accepted 08 February 2017

Online 3 March 2017

Keywords:

Tube girder;

C-Mn steel;

Welding technology;

Hardness;

Microstructure.

Available online: <http://fstroj.uniza.sk/journal-mi/PDF/2016/04-2017.pdf>

ISSN 1335-0803 (print version)

ISSN 1338-6174 (online version)

1. Introduction

The objective of the research, reported in this paper, was to determine which technology should be used for welding the cover onto the tube made of the C-Mn steel. The welded tube girder is a part of the assembly of the large hadron collider (LHC) of the largest accelerator made under the auspices of CERN. According to Fig. 1 the tube and the cover should be welded over the whole perimeter (Fig. 1a) with previously prepared groove (detail "A" in Fig. 1b).

Since this is an extremely responsible structure, the selection of the welding procedure must be preceded by verifying the base metal's chemical composition and mechanical properties, despite the declaration provided by the steel's manufacturer. This should be done

before the welding of any responsible part since the possibility always exists that the data provided do not correspond to actual properties or composition of the delivered steel, what could cause problems in the part's exploitation, or even the catastrophic fracture [1].

2. Estimates of the base metal's weldability

The chemical composition and the mechanical properties of steel L355 (EN) i.e. St 52.0 (DIN), certified by the manufacturer and obtained by the chemical analysis, are presented in Table 1 [2, 3]. Obtained and prescribed values are in agreement with the corresponding standard values for this type of steel, DIN 1629-84.

Based on the chemical analysis of the welded steel and microscopic examination it was established that this

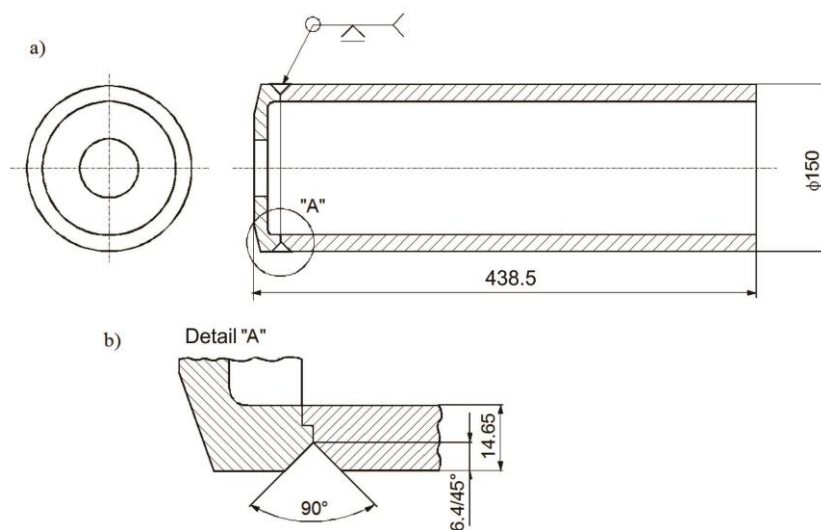


Fig. 1. Welding of the tube and its cover (a) and appearance of the groove (b).

Table 1

Chemical composition and mechanical properties of HSS L355 (St 52.0).

Chemical composition (wt. %)									
	C	Si	Mn	P	S	Cr	Ni	Cu	Al
Catalogue	0.14-0.20	0.4-0.55	1.2-1.5	≤0.040	≤0.04	≤0.30	≤0.30	≤0.03	-
Analyzed	0.17	0.45	1.33	0.008	0.009	-	-	-	0.028
Mechanical properties									
	Yield stress R_{eH} (MPa)		Tensile strength R_m (MPa)			Elongation A_5 (%)			
Catalogue	min 355		500-650			min 21			
Analyzed	377		577			30.8			

is the fine-grained C-Mn steel of the ferrite-pearlite structure.

Prior to selecting the welding process, technology and eventual heat treatment (before or after the welding), it is necessary to estimate the weldability of this base metal [4 - 6].

2.1 Chemically equivalent carbon

The chemically equivalent carbon (CE) for this type of steels is calculated according to the following expression [7, 16]:

$$CE = C + \frac{Mn}{6} + \frac{Cr + Mo + V}{5} + \frac{Ni + Cu}{15}, \% \quad (1)$$

Steels with value of $CE > 0.45$ % are considered as conditionally weldable

(the application of the prior and post welding heat treatments is necessary – preheating and tempering), while the steels with value of $CE \leq 0.45$ % are considered as well weldable.

After substituting the corresponding values for all the chemical elements in expression (1), the obtained value of chemically equivalent carbon was $CE = 0.392$ %, what is obviously less than 0.45 %. Thus, this steel can be considered as well weldable.

However, after the weldability estimate, based on the equivalent carbon, due to extreme responsibility of this welded assembly and the whole structure, the checking of this steel's tendency towards creation of the hot and cold cracks during the welding was performed.

2.2 Parametric equations for evaluation of the steels tendency towards creation of cracks

2.2.1 Parametric equations for evaluation of tendency towards creation of cold cracks

For estimates of the C-Mn steel's tendency towards creation of cold cracks (when the yield strength is between 272 and 870 MPa), one applies equations that take into account the following parameters: *chemical composition* of the base metal and the *content of the diffused hydrogen*, as well as the *stiffness* and the *thickness* of the welded joint.

According to Prochazka et al. [8], the following equations should be applied:

$$P_{hp} = P_{CM} + \frac{K}{40000} + 0.015 \cdot \log \frac{H}{2.77}, \text{ for } K \leq 1300 \quad (2)$$

$$P_{hp} = P_{CM} + \frac{K}{40000} + 0.075 \cdot \log \frac{H}{2.77}, \text{ for } K > 1300 \quad (3)$$

$$P_{CM} = C + \frac{Si}{30} + \frac{Mn + Cu + Cr}{5} + \frac{Ni}{60} + \frac{Mo + V}{15} + 5 \cdot B \quad (4)$$

where: $K = 70 \cdot s$ – is the stiffness factor of the but joints, s , mm , is the welded material thickness and H , $cm^3 / 100 g$, is the content of the diffused hydrogen in the weld metal.

The welded joint, for which the obtained value of P_{hp} is ≤ 0.24 is considered as resistant to cold cracks, while for the values of $P_{hp} > 0.24$ the preheating is necessary to temperature of:

$$T_p = 1600 \cdot P_{hp} - 308, ^\circ C \quad (5)$$

Under the assumption that the welding would be done in the protective gas atmosphere (80% Ar + 20% CO₂), with the dry and clean wire, value $H = 3 ml/100 g$ was adopted. The maximum thickness of the welded part is $s = 14.65 mm$. According to those assumptions, the following values were obtained:

$K = 1025.25 < 1300$, $P_{CM} = 0.2515$, $P_{hp} = 0.278$, namely $T_p = 136 ^\circ C$.

Analogously to formula for the chemically equivalent carbon, the indicator of tendency of the low alloyed steels towards creation of cold cracks during the welding could be calculated as [7]:

$$P_C = P_{CM} + \frac{S}{600} + \frac{H}{60} \quad (6)$$

where:

$$P_{CM} = C + \frac{V}{10} + \frac{Mo}{15} + \frac{Mn + Cu + Cr}{20} + \frac{Ni}{60} + 5 \cdot B \quad (7)$$

If the value of P_C is obtained to be within range $0.25 < P_C < 0.40$, at the medium driving energy, then the preheating is necessary, at temperature:

$$T_p = 1440 \cdot P_C - 392, ^\circ C \quad (8)$$

With the same input parameters as for the previous estimate (expressions (2) to (5)), the following values were obtained:

$P_{CM} = 0.2365$, $P_C = 0.3109$, namely $T_p = 56 ^\circ C$.

The preheating temperature, for the conditionally weldable steels, could be also calculated according to expression, proposed by Seferian [9]:

$$T_p = 350 \cdot \sqrt{[C] - 0.25}, ^\circ C \quad (9)$$

$$[C] = [C]_h + [C]_s = [C]_h(1 + 0.005 \cdot s), ^\circ C \quad (10)$$

$$[C]_h = C + \frac{Mn + Cr}{9} + \frac{Ni}{18} + \frac{7 \cdot Mo}{90}, ^\circ C \quad (11)$$

With the same input data as before the following values were obtained:

$[C]_h = 0.317$, $[C] = 0.34$, namely $T_p = 105 ^\circ C$.

However, taking into account that the first (root) pass is the most important

for obtaining the optimum structure of all the zones of the welded joint, somewhat higher preheating temperature, $T_{pmax} = 150 \text{ }^\circ\text{C}$, was adopted for the test welding.

So the conclusion is that this steel is resistant to cold cracks, with application of preheating.

2.2.2 Parametric equations for evaluation of tendency towards creation of hot cracks

According to [7], tendency towards creation of hot cracks can be estimated according to the modified equivalent carbon:

$$CE_m = C + 2 \cdot S + \frac{Si - 0.4}{10} + \frac{Mn - 0.8}{12} + \frac{Ni}{12} + \frac{Cu}{15} + \frac{Cr - 0.8}{15}, \% \quad (12)$$

Steels that have the value $CE_m > 0.45\%$ are prone to creating the hot cracks and vice versa.

Ito and Bessyo [10] have derived the following expression for estimates of tendency for creating the hot cracks, the so-called Hot Cracks Sensitivity factor – HCS :

$$HCS = \frac{C \cdot (S + P + \frac{Si}{25} + \frac{Ni}{100}) \cdot 10^3}{3 \cdot Mn + Cr + Mo + V} \quad (13)$$

The permissible value of the HCS depends on the type of steel. Thus, for the carbon steels that are prone to creating the hot cracks the value should be $HCS > 4$, while for the high strength steels it amounts to $HCS > 2$ for thin sheets and $HCS > 1.6$ for thick sheets.

According to expressions (12) and (13),

with the same input data as for previous calculations, the following values were obtained: $CE_m = 0.237 < 0.45$ and $HCS = 1.49 < 1.6$, which implies that the base metal St 52.0 is resistant to hot cracks.

3. Selection of the procedure and the technology of welding

The welding procedure selection for this type of steels should include all the factors that would eventually lead to desired properties of the welded joint, primarily its strength and favorable microstructure. Based on previous research by this group of authors [11 - 13] and material properties defined in the previous sections, as well as on the mentioned requirements for the welded joint properties, the selected procedure was welding in the protective gas atmosphere (gas mixture 80 % Ar + 20 % CO₂), on the semi-automatic programmed machine for the circular welding. Since this welding had to be executed with maximal precision, to avoid the influence of the radial deformations of the cover and the tube during the welding, their proper positions had to be secured. Thus, the two parts were fixed in the adequate mutual position with the three fixing welds, at 120° distances, Fig. 2.

The fixing welding was done in the CO₂ protective atmosphere (CO₂ - GMAW), with the wire of diameter 1.2 mm and current $I \approx 200 \text{ A}$, while the length of welds was 20 mm. After the cooling to the room temperature, the beginnings and the ends of all the three welds were ground.

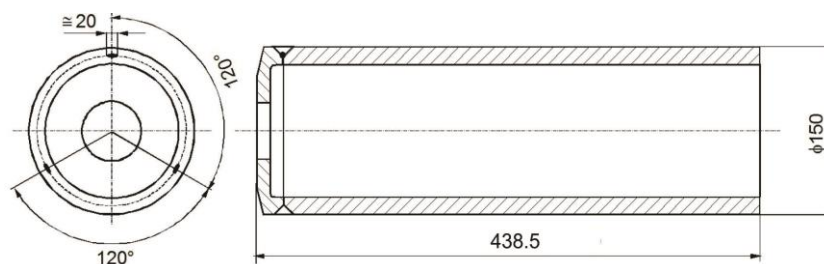


Fig. 2. Schematic presentation of the cover to tube fixing-welding.

3.1 The technological welding parameters

The following technological parameters of welding in the protective gas atmosphere were applied:

- Groove area

$$A_z = 2 \cdot P_\Delta = 2 \cdot \frac{6.4 \cdot 6.4}{2} = 40.96 \text{ mm}^2$$

- Weld area

$$A_w \approx 1.2 \cdot A_z = 1.3 \cdot 40.96 = 53.248 \text{ mm}^2$$

- Area of a single weld

$$A_{sw} \approx 25 \text{ mm}^2$$

- Weld's mass per unit length

$$M = \rho \cdot A_z \cdot L = 7.85 \frac{\text{g}}{\text{cm}^3} \cdot 0.25 \text{ cm}^2 \cdot 1 \text{ cm} = 1.9625 \text{ g}$$

- Deposited material mass per time unit

$$m_{1.6} = 0.64 + 0.55 \cdot M - 0.055 \cdot M^2 \approx 1.51 \text{ g/s}$$

- Welding speed

$$v_w = \frac{m \cdot 6000}{A_z \cdot \rho} = \frac{1.51 \cdot 6000}{25 \cdot 7.85} = 46 \text{ cm/min} = 0.768 \text{ cm/s}$$

- Wire melting rate

$$v_m = \frac{0.012732 \cdot A_z \cdot v_z}{d^2} = \frac{0.012732 \cdot 25 \cdot 46}{1.6^2} = 5.7 \text{ m/min}$$

- Welding current intensity

$$I_{1.6} = 378 \cdot \log v_i + 26 = 378 \cdot \log 5.7 + 26 \approx 312 \text{ A}$$

- Welding current polarity

DC (E+)

- Working voltage

$$U = 14 + 0.05 \cdot I = 14 + 0.05 \cdot 312 \approx 30 \text{ V}$$

- Welding input heat

$$q_t = \frac{U \cdot I}{v_z} \cdot \eta = \frac{30 \cdot 312}{0.768} \cdot 0.85 = 10359 \text{ J/cm}$$

- Welding depth

$$\delta = 0.3 \cdot r = 0.3 \cdot 0.00537 \cdot \sqrt{q_t} = 0.3 \cdot 0.00537 \cdot \sqrt{10359} = 1.64 \text{ mm}$$

- Protective gas type
mixture (80% Ar + 20% CO₂)

- Protective gas flow rate
 $q \approx 18 \text{ l/min}$

Besides those technological parameters, one should also consider the following: the length of the drawn wire, the position of the electrode with respect to the joining plane, the distance of the gas nozzle from the working piece surface, polarity of the wire electrode, welding position, variable inductance, etc.

The calculated welding parameters serve as the initial ones in selecting the welding regime in protective gas atmosphere. They are being compared to parameters proposed from experience so that the eventual correction could be done before the actual welding is executed. After investigating the test welds, one should adopt the welding parameters that produce the best results.

3.2 The filler metal selection

Based on the authors' previous experience and recommendations from the electrodes' manufacturers, the steel (copper plated) wire VAC 60, $\emptyset = 1.6 \text{ mm}$ (SRPS C.H3 Č3203; EN ISO 14341, DIN 8559/94 SG-2-CY 4233; AWS A5.-18-79 ER 70S-6) was used as the filler metal [14]. It is aimed for welding in the protective gas atmosphere. According to the manufacturer's recommendation this wire is adequate for welding of the non-alloyed and low-alloyed structural steels with strength up to $R_m = 590 \text{ MPa}$, boiler thin sheets, ship thin sheets etc.

Table 2

Mechanical properties of the pure weld.			
Yield stress $R_{p0.2}$ (MPa)	Tensile strength R_m (MPa)	Elongation A_5 (%)	Toughness (- 40 °C) ISO-V (J)
410-490	510-590	22-30	> 47

Mechanical properties of the pure weld metal and the chemical composition of the wire are given in Tables 2 and 3, respectively.

Table 3

Chemical composition of the wire (wt. %).

C	Si	Mn	P	S
0.08	0.90	1.50	<0.025	<0.025

3.3 Preparation and control of samples for test welding

As already emphasized, due to necessary precise executing of the welds, both on the test samples and on the real assembly, the circular radial deviation of each working piece was controlled (Fig. 3a). This deviation was within the range 0.1 to 0.2 mm, what was considered as acceptable. In addition, before the welding the fixed pieces were degreased by washing with an appropriate detergent and then dried.

To be sure that the adopted welding technology was the optimal one, numerous test welds were executed with the calculated welding parameters, in conditions with preheating ($T_p = 150$ °C) and without the preheating, with three (Fig. 3b) and two passes (Fig. 3c).

From the tested welded pieces, the metallographic samples were then prepared by grinding. They served for measuring the micro hardness (HV1) and for checking the micro structure of all the zones of the welded joint. The macro structure was evaluated by eye examination and the results were completely satisfactory for the welding joints testing standards.

4. Results and discussion

Results of the hardness measurements in the individual zones of the welded joint and the obtained corresponding micro structures are shown in Table 4.

Hardness distribution and appearance of micro structures for the two-layer and three-pass welding are presented in Figs. 4 and 5,

respectively (hardness measurement direction is the I-I direction shown in Figs. 3b and 3c).

Analysis of obtained results led to conclusion that no major differences were spotted either in values of measured hardness or in the microstructures in individual zones of the welded joint for the cases of welding with and without the preheating, both for the two or three layer welding. Welding of the cover to the tube with three passes (with or without preheating) was done primarily because of the large angle of the groove opening and necessary post treatment of the weld's face. The passes were executed immediately one after the other (Fig. 3b). The cover pass 2 tempers the root cover 1 and the cover pass 3 tempers the root pass 1 and partially the pass 2, as well. That produces significantly more favorable microstructure, avoids creation of the possible brittle phases and reduces the level of residual stresses, as well. With this type of welding the necessary overfill of the welded joint was created, which was later removed by machining for the final ultrasonic control.

During the welding the parameters, related to the driving energy of welding (power I , voltage U and the welding velocity v_w), were constantly monitored. The energy was within limits $q_l = 9500-10500$ J.cm⁻¹. It provided the necessary welding penetration, favorable hardness and micro structure, as well as the adequate output mechanical properties of the welded joint.

Experimental investigations have confirmed that the base metal was the well weldable steel, thus either the previous or the additional heat treatment were not necessary. The preheating was applied as a precautionary measure to prevent formation of cracks and to lower the level of residual stresses in the HAZ.

Apart from the visual control and conducted metallographic tests, each welded joint on real parts was controlled by the ultrasonic defectoscopy in the laboratory, which was accredited for the non-destructive

testing. In all the performed investigations, no flaws, external or internal, were noticed in the welded joints.

Besides the described experimental investigation, an additional checking if the adopted procedure and the welding parameters were adequate to ensure the favorable structure and mechanical properties of the welded joint (optimal toughness, adequate hardness, etc.), could be done by analyzing the continuous cooling diagram (CCT) of the steel,

in the welding conditions. The characteristic cooling time between 800 °C and 500 °C ($t_{8/5}$), calculated according to empirical formula of Ito and Bessyo [10], would be entered into the CCT diagram. That would enable estimating of the microstructure, as well as reading-off the hardness and toughness of the HAZ, [11 - 13].

This analysis was not performed within this research since all the other parameters were showing that the selected welding procedure and technology were adequate.

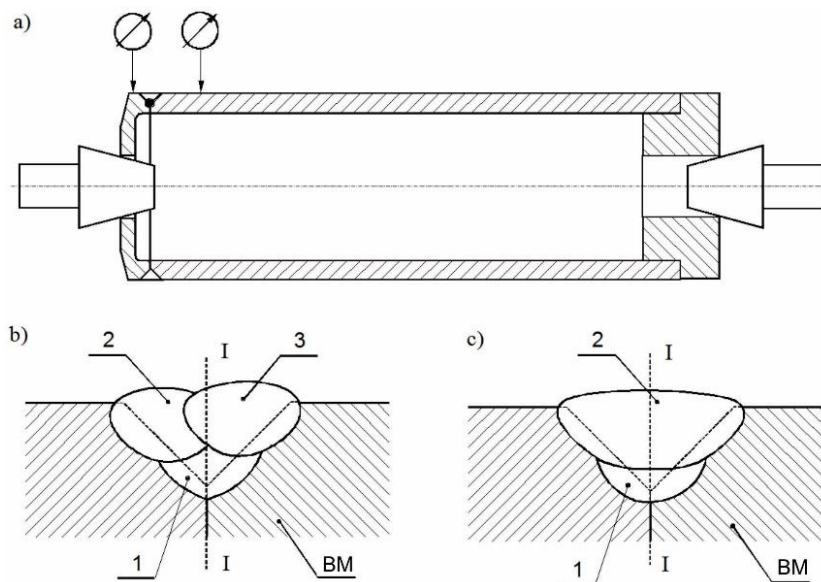


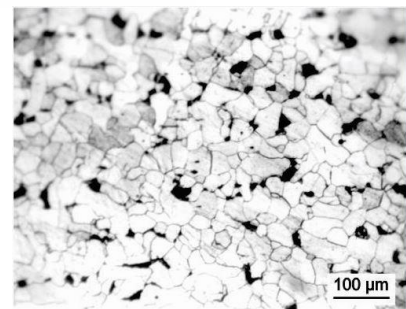
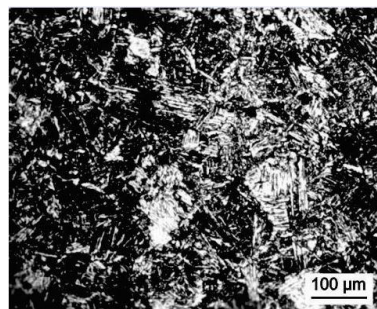
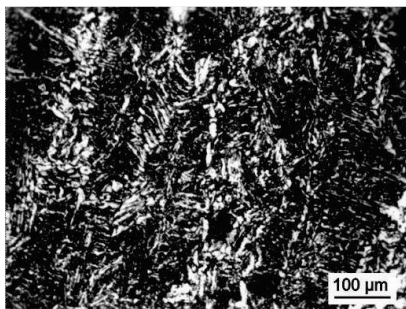
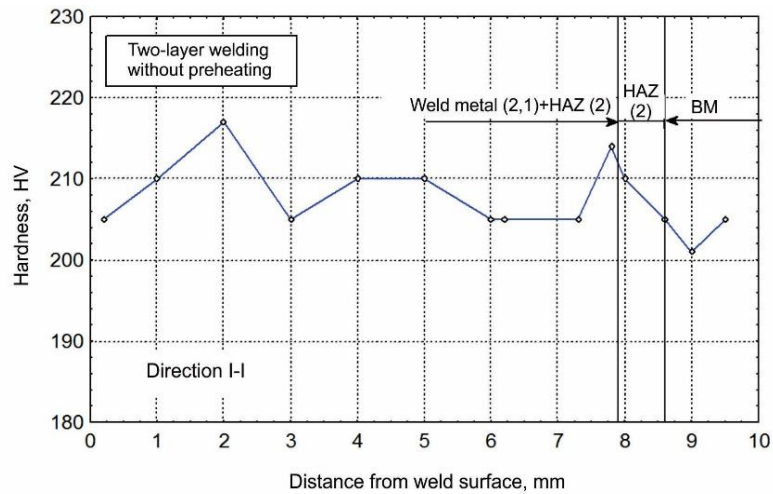
Fig. 3. Schematic presentation of the circular deviation control (a); of the three-pass welding (b) and the two-layer welding (c).

Table 4

Measured hardness and microstructures of the welded joint individual zones.

Number of layers/passes	Preheating temperature (°C)	Maximal and minimal hardness (HV1) and Determined microstructure*		
		Weld metal	HAZ _{3,2,1} and HAZ _{2,1}	BM
3 passes	$T_p \approx 150$ °C	221-251 HV1	210-227 HV1	201-210 HV1
		Fine grained Widmannstetten	Interphase + tempered martensite	Lamellar pearlite- ferrite
2 layers	$T_p \approx 20$ °C	205-217 HV1	205-214 HV1	201-210 HV1
		Fine grained Widmannstetten	Interphase + tempered martensite	Lamellar pearlite- ferrite
3 passes	$T_p \approx 20$ °C	201-234 HV1	219-229 HV1	201-210 HV1
		Fine grained Widmannstetten	Interphase + tempered martensite	Lamellar pearlite- ferrite

*Respective microstructures are shown in Figs. 4a to 4c and 5a to 5c. Structures in Figs. 4c and 5c are practically the same since due to the input heat the structures were unified.

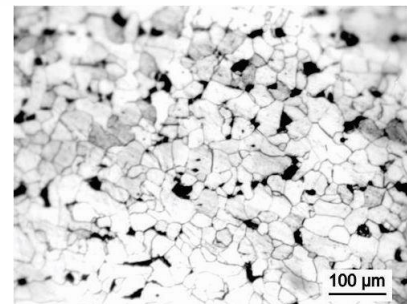
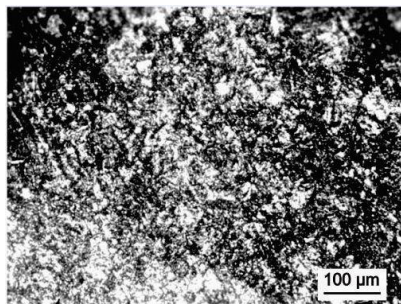
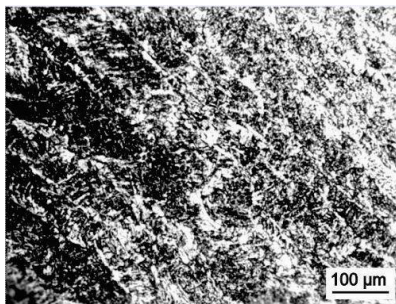
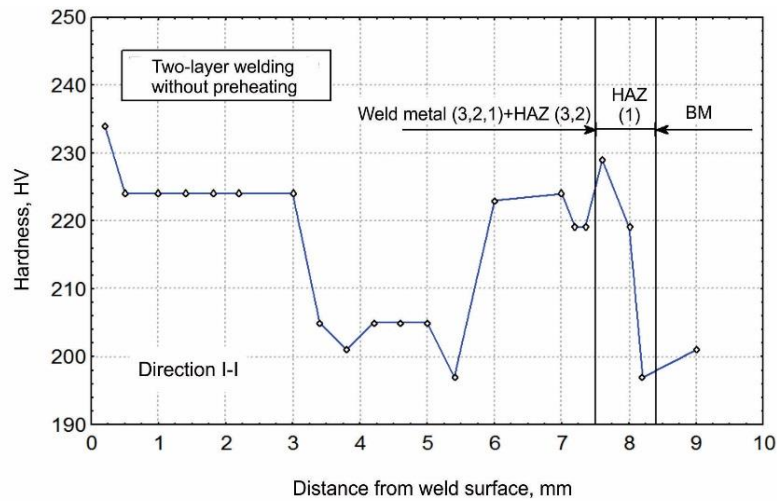


a) weld metal - fine grained Widmannstetten

b) HAZ - interphase + tempered martensite

c) BM (tube) - lamellar pearlite-ferrite

Fig. 4. Hardness distribution and appearance of micro structures in the two-layer welding.



a) weld metal - fine grained Widmannstetten

b) HAZ - interphase + tempered martensite

c) BM (tube) - lamellar pearlite-ferrite

Fig. 5. Hardness distribution and appearance of micro structures in the three-pass welding.

5. Conclusions

Based on the conducted theoretical and experimental analysis, related to weldability of the base metal, adopted procedure, chosen filler metal, applied technology and control of the welded joints, the following conclusions were drawn:

- The base metal is from the class of the medium to high strength steels and it belongs to a group of the well weldable steels (with application of preheating if necessary);
- This steel is not prone to creation of either cold or hot cracks during the welding;
- This steel is not prone to creation of brittle phases during the welding;
- Welding can be successfully executed in the protective gas atmosphere (mixture 80 % Ar + 20 % CO₂) with the proposed procedure and technological parameters;
- The three-pass welding is necessary due to structurally required type of the groove (too large groove opening);
- Neither unfavorable structures nor the zones of increased hardness were noticed during the experimental investigations;
- All the welded joints on the real parts were controlled by the ultrasonic defectoscopy and no flaws, external or internal, were registered.

Acknowledgements

This research was partially financially supported by the European regional development fund and Slovak state budget by the project "Research Centre of the University of Žilina" – ITMS 26220220183 and by the Ministry of Education, Science and Technological Development of Republic of Serbia through grants: ON174004, TR35024 and TR33015.

Note: *The shorter version of this research was presented at the 44th International Conference "ZVARANIE 2016", reference [15].*

References

- [1] M. Matejić, R. R. Nikolić: Mater. Eng. - Mater. Inž. 21(4) (2014) 178-184.
- [2] EN 10224: 2002 Non-alloy steel tubes and fittings for the conveyance of water and other aqueous liquids. Technical delivery conditions.
- [3] DIN 1629-84: Seamless circular tubes of non-alloy steels with special quality requirements.
- [4] D. Arsić, V. Lazić, R. Nikolić, S. Aleksandrović, B. Hadzima, M. Djordjević: Mater. Eng. - Mater. Inž. 22(1) (2015) 33-47.
- [5] D. Arsić, R. Nikolić, V. Lazić, B. Hadzima, S. Aleksandrović, M. Djordjević: In Proc. of 42. International Conference Zvaranie 2014, Tatranská Lomnica, Slovakia, 2014, pp. 11-21.
- [6] D. Arsić, M. Djordjević, V. Lazić, S. Aleksandrović, R. Nikolić: In Proc. of 19th International PhD. students' seminar SEMDOK 2014, Žilina-Terchová, Slovakia, 2014, pp. 5-9.
- [7] J. Prochazka et al.: Technologie slevani tvareni a svarovani – Ediční středisko ČVUT, Praha, 1985.
- [8] D. Seferian: Metallurgie de la soudure, Dunod, Paris, 1965.
- [9] M. Jovanović, V. Lazić, D. Adamović: Technology of welding, Handbook, Faculty of Mechanical Engineering in Kragujevac, Kragujevac, 2011.
- [10] Y. Ito, K. Bessyo: Journal of Iron and Steel Institute (13) (1972) 916-930.
- [11] R. Vulović, V. Lazić, M. Jovanović, R. Nikolić, D. Adamović: In Proc. of The Fifth International Conference "Heavy Machinery HM", Kraljevo, 28 June – 03 July 2005, pp. II A.17-20.
- [12] D. Arsić, M. Djordjević, V. Lazić, S. Aleksandrović, R. Nikolić: In Proc. of SEMDOK 2014, Edited by P. Palček, Terchova, Slovakia, 29-31 January, 2014, pp. 5-9.
- [13] D. Arsić, R. Nikolić, V. Lazić, B. Hadzima, S. Aleksandrović, M. Djordjević: In Proc. of 42. International Conference "Zvaranie 2014", Tatranská Lomnica, Slovakia, 2014, pp. 11-21.
- [14] Catalogues of base and filler metals (welding consumables): Steel plant Jesenice, Slovenia; EN Standards; DIN normen.
- [15] V. Lazić, D. Arsić, R. Nikolić, S. Aleksandrović, M. Djordjević, B. Hadzima:

In Proc. of 44th International Conference "Zvaranie 2016", 09. – 11. November 2016, Tatranska Lomnica, Slovakia.

[16] EN 1011-2: Welding — Recommendations for welding of metallic materials — Part 2: Arc welding of ferritic steels, British Standard.